

Optofluidic Sorting Of Ultra-Bright Nanodiamonds

By

James White

A thesis submitted to Macquarie University

for the degree of Master of Research

Department of Engineering

November 2017



MACQUARIE
University
SYDNEY • AUSTRALIA

Except where acknowledged in the customary manner, the material presented in this thesis is, to the best of my knowledge, original and has not been submitted in whole or part for a degree in any university.

James White

Acknowledgements

David Inglis, Shilun Feng, Lianmei Jiang, Thomas Volz, Matt van Breugel, Carlo Bradac, Nabomita Roy Mukty, Reece Roberts, Louise Brown, Ajay Hasija, Peter Dekker, Benjamin Johnston, Alex Stokes, Simon Doe and Donghoon Chang. This work was performed in-part at the OptoFab node of the Australian National Fabrication Facility, utilising NCRIS and (NSW) state government funding.

Thank you to my Family and Friends for your irrevocable love.

Abstract

Biological imaging will advance when fluorescent markers overcome the limitations of toxicity and photo instability. Recent work by Brown [31] indicates that fluorescent nanodiamonds avoid these limitations, as the carbon composition of the diamond removes toxicity and the embedding of defects in the diamond lattice increases photo stability. A current restriction to the use of nanodiamonds in imaging applications is the brightness variations from particle-to-particle [14]. A new project at Macquarie University intends to improve the brightness uniformity of nanodiamond materials, using a sorting mechanism that impacts the defects embedded in the diamond. This thesis works towards the aims of the recently funded Discovery Project (DP170103010) to quantify the impact that defect variations have on the scattering force effect, and to develop a system for enriching the brightest particles. Fulfilling this aim required the development of a microfluidic device with an observable micro-channel and orthogonal laser accessibility. An optical setup was established to direct a high powered laser at a sample of particles that were suspended inside the channel. Microscopic images were recorded and the trajectories of each particle were tracked and recorded to quantify the behaviour of the impacted particles [1].

Contents

Acknowledgements	v
Abstract	vii
Contents	ix
1 Introduction	1
1.1 Project Scope	1
1.2 Project Direction	1
1.3 Document Structure	2
2 Background and Related Work	3
2.1 Fluorescent Nanodiamonds	3
2.1.1 Background	3
2.1.2 Properties	4
2.1.3 Limitations	4
2.2 Particle Sorting Mechanisms	4
2.2.1 Fluorescent Activated Cell Sorters	4
2.2.2 Open Loop Sorting Mechaisms	5
2.2.3 Label-Free Sorting	6
2.2.4 Label-Free Optical Sorting by Brightness	6
2.3 Optical Theory	8
2.3.1 Estimation of Scattering Force	8
2.3.2 Sorting Mechanism	10

2.3.3	Cooperative Effects	12
2.4	Microfluidic Engineering	13
2.4.1	Background	13
2.4.2	Fabrication Processes	13
2.5	Previous Work	16
2.6	Chapter Summary	16
3	Microfluidic Fabrication	17
3.1	Problem Definition	17
3.2	Design Description	17
3.3	Processes of Microfluidic Fabrication	19
3.3.1	PDMS Moulded Devices	20
3.3.2	Laser Etched Borofloat33	22
3.3.3	Deep Reactive Ion Etched Glass	23
3.4	Device Overview	24
3.5	Scanning Electron Microscopy	25
3.6	Discussion	27
3.7	Chapter Summary	27
4	Optical Configuration	29
4.1	Experiment Introduction	29
4.2	Particle Selection	29
4.3	Chuck Design	30
4.4	Optical Theory	30
4.5	Configuration of Optical Elements	32
4.5.1	Components	32
4.5.2	Optical Path	32
4.6	Discussion	32
4.7	Chapter Summary	33
5	Results	35
5.1	Hypotheses and Expected Results	35
5.2	Optical Coupling Experiment	35

5.3	Laser Scattering Force Measurement	38
5.4	Processing of Tracking Results	41
5.4.1	Matlab Output	41
5.4.2	Calculation of Scattering Force	43
5.4.3	Calculation of Intensity Distribution	44
5.4.4	Calculation of the Scattering Cross Section	44
5.5	Discussion	46
5.6	Chapter Summary	46
6	Conclusion	47
	References	49

1

Introduction

1.1 Project Scope

Biology needs a small bright probe to understand how biological systems function at the molecular level. This probe must have an emission that is distinct from the autofluorescence of the surrounding tissue. Popular nanometer fluorescent markers are limited by their toxicity and photo instability. Fluorescent nanodiamonds overcome these limitations, as the carbon composition is non-toxic [2] and the embedded defects are photo stable [3]. The irregularity of defect formation introduces non-uniformity to the fluorescent brightness of nanodiamonds, which is the primary limitation to their use as a probe. The inability to synthesise nanodiamonds with brightness uniformity introduces the need for a mechanism that can efficiently sort bright and dark nanodiamonds.

1.2 Project Direction

Our aim is to determine whether multiple lasers can be used to impact only the brighter nanodiamonds in an inhomogeneous stream. This requires:

- The design and fabrication of an optofluidic sorting environment,
- An optical configuration that can isolate a defect dependent effect,
- An understanding of the scattering force related to distinct nanodiamond brightnesses.

In this thesis we developed an optofluidic environment to observe and quantify the scattering force delivered by our optical configuration. Future contributors will need to remove the size dependent effects to characterise the effect of defect dependent scattering forces.

1.3 Document Structure

This thesis is broken into chapters that encompass stages of the projects development.

Chapter 2 is a review of fluorescent nanodiamonds, particle sorting methods, optical theory and microfluidic engineering that contextualises the project to highlight the novelty of the sorting mechanism, and ultra-bright nanodiamonds.

Chapter 3 provides an examination of the design and fabrication of a microfluidic environment. This chapter outlines the process and considerations that determined the ability of the optofluidic device to sort nanodiamonds based on a criterion of brightness.

Chapter 4 details the design and configuration of the optical system used to impact the optofluidic device with scattering forces. This chapter summarises the components, materials and revisions that defined the optical setup.

Chapter 5 delivers a quantification of the systems performance. This chapter analyses the coupling experiment and scattering experiment to understand the particles response to a scattering force.

Chapter 6 contains the conclusions and future considerations of this work.

2

Background and Related Work

This thesis aimed to develop an environment where optical forces could be used to impact and ultimately sort nanodiamond materials using a brightness criterion. This chapter aims to contextualise the project within fluorescent nanodiamond research, particle sorting mechanisms, optical theory and microfluidic engineering.

2.1 Fluorescent Nanodiamonds

2.1.1 Background

Nanodiamonds (NDs) are nanoscale carbon crystals that exhibit a range of promising characteristics for bio applications. These characteristics have created a demand for synthetic productions that return higher ND yields than are naturally occurring. To produce NDs there are many different growth techniques, including:

- Chemical Vapour Deposition which uses a mixture of hydrogen and hydrocarbon gas to synthetically grow NDs on a substrate [4].

- High Pressure, High Temperature (HPHT) synthesis, transforms graphite into diamond through an exposure to increased pressure and temperature. The HPHT method requires further processing (grinding/milling) to reduce the size of the diamond to a ND [5].
- Detonation synthesis explodes carbon materials in a detonation chamber to increase the temperature and pressure conditions to a point that forms ND pieces [6].

Synthetically produced ND particles often require further processing to clean the sample, remove residual graphite, disperse aggregates, and reduce the size variations that are related to the irregularity of ND formation [7].

Fluorescent NDs (FNDs) have defects that act as fluorophores embedded in the crystal lattice of the ND. These defects disrupt the regular diamond lattice when displaced carbon atoms are substituted with elementary impurities [8]. Colour centres define the effect an embedded impurity has on the diamonds absorption range [9]. Most publications focus on the commonly occurring Nitrogen Vacancy (NV) centre, but our project is interested in the superior optical qualities of the Silicon Vacancy (SiV) centre [10].

2.1.2 Properties

The combination of the physical and optical properties of FNDs are exciting for bio applications that require fluorescent probes. The primarily carbon composition is non-toxic and biocompatible across multiple cell lines for both in vivo and in vitro use [11, 12]. The adaptable surface chemistry of ND is a property that is well suited to applications where probes are attached, functional groups can be bonded to the surface of the FND and these groups can be attached to proteins, DNA or drugs (in delivery applications) [13, 14].

The photostability of FNDs is the most significant property in imaging applications, as the fluorescent defects that are embedded in the colour centres of a FND probe do not typically experience photo bleaching or photo blinking [15]. This photostability separates FND particles from other probes, as it extends the observation period that can be achieved within living tissue. The relative brightness of FND particles is also significantly higher than the brightness of other probes that exhibit a distinct emission within living tissue [16].

2.1.3 Limitations

The impact of a FND sample processed for both size and brightness uniformity is significant, as the resulting probe could conduct quantitative analysis and image sub-cellular processes [17]. Variations in FND size have led researchers to sort the material with centrifugation. The particle-to-particle variations in brightness are harder to accommodate as the fluorescent defects appear irregularly within ND.

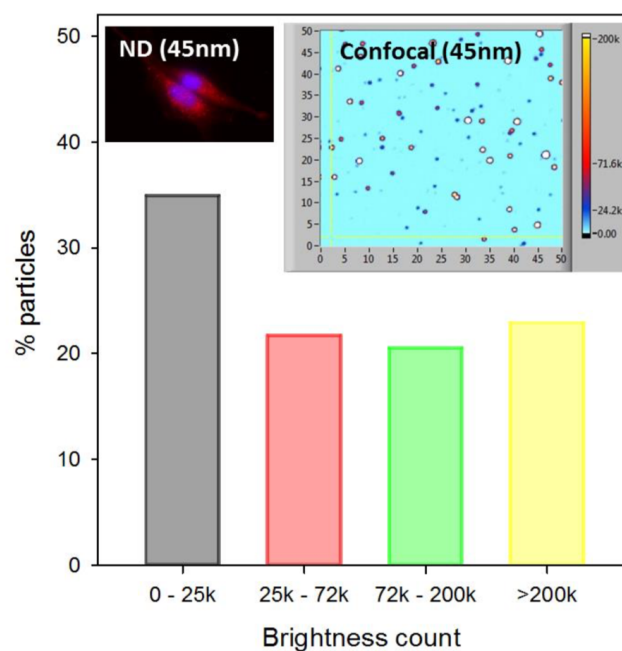


Figure 2.1: Typical distribution of the brightness levels associated with 45 nm ND, the column graph shows the range of brightnesses associated with a single size of ND. (unpublished image courtesy of Louise J. Brown).

Controlled growth synthesis, ion implantation, and irradiation are processes that increase the fluorescence of NDs, by interrupting the regular lattice and embedding colour centres within the crystal [18]. These methods are expensive and produce small FND yields that do not exhibit brightness uniformity. Figure 2.1 shows the brightness variations for FNDs that were sorted by size before irradiation increased the density of defects. The inability to fabricate a FND sample that exhibits brightness uniformity creates a demand for a sorting mechanism that is able to sort existing materials using a brightness based force.

2.2 Particle Sorting Mechanisms

2.2.1 Fluorescent Activated Cell Sorters

Sorting procedures are used to isolate particles with a selected characteristic from an inhomogeneous sample. In a laboratory environment these procedures are predominantly performed by a Fluorescent Activated Cell Sorter (FACS). FACS systems typically require the preparation of the unsorted sample, this preparation attaches a marker to particles that exhibit the selected characteristic. This marker is often an antibody that specifically binds to proteins present on the cell or target surface. FACS uses fluorescent markers and scattered light to distinguish the particles. The particles are then placed in droplets and serially sorted based on the optical features of the marker. Most conventional cell sorters use electrostatic forces on a charged droplet to activate the sorting mechanism, but many methods have been demonstrated [19].

Optical forces could potentially be used in these systems to actively sort the tagged particles. The systems could use the ability of an optical trap to control the path of selected particles by steering the tagged particle into a target stream of fluid [20]. Optical traps that operate over a line have also been used to sort particles, operating as an optical switch that interrupts the path of selected particles, redirecting these particles into the target stream based on a fluorescent selection [21].

2.2.2 Open Loop Sorting Mechanisms

The sorting mechanism that we are interested in needs to be able to sort a large number of NDs because of the tiny size (100 nm) there are $\sim 10^{14}$ NDs per milligram. Closed loop, active sorting methods like FACS, which interrogate each particle and make a decision before actively sorting certain particles are currently limited to around 60,000 sorts per second. At this rate it would take years to sort even milligrams of a ND product [22].

Open loop sorting provides an efficient sorting mechanism without an expensive apparatus. These sorting methods use an intrinsic (label free) or extrinsic (added label) characteristic of the target cell to selectively sort the cells in the solution [19]. Magnetic markers are the most common example; wherein magnetic beads are attached to particles in the sorting process to control the path of the targeted particles (MACS: Magnetically Activated Cell Sorting) [23]. This method removes the serial interrogation limitation encountered by FAC systems to enable the processing of many more than 60,000 sorts per second.

2.2.3 Label-Free Sorting

Sorting of NDs for brightness is a unique challenge as bright and dark particles may have the exact same chemical composition. It is therefore difficult to see a method of selectively attaching a label to the bright particles and not the dark ones. This limitation encourages the use of an intrinsic or label free sorting method. There are a range of label-free sorting mechanisms that use physical properties to sort; density in centrifugation [24], size-based methods such as deterministic lateral displacement (DLD) [25] and membrane filtration [26], dielectric properties [27, 28], or intrinsic magnetic susceptibility [29], to name a few. Inertial forces in a spiralled channel can be used to isolate circulating tumour cells by exploiting the size dependence of the centripetal effect. The collection ports at the edge of the device, collected particles of different sizes as they spiral [24]. DLD arrays use a grid of obstacles to direct a particle's path based on its geometry. Membrane filtration sorters have a similar mode of operation to DLD arrays as they separate particles using size to direct the particles path inside the device [26].

Gradient based separation techniques use intrinsic responses to gradient conditions to sort particles using the attractive or repulsive effect of the force. These systems revolve around a size dependent effect that separates the particles using the extremes of the gradient. The systems are then designed to collect the samples at the gradient extremes. Magnetic [29], acoustic [28], electric [27], and chemical [30] sorters have been designed using this principle.

2.2.4 Label-Free Optical Sorting by Brightness

None of these label-free or intrinsic methods offer a mechanism that is capable of sorting bright FNDs from dark FNDs, but optical forces do. A number of optical sorting devices use the absorbance relationship that links resonance to a transfer of momentum, by relating the movements of different particle sizes to the wavelength of illumination. For example, pure scattering caused by a non-absorbing particle that is significantly smaller than the illumination wavelength, and has an index of refraction that is different from its surrounding medium, experiences a scattering force that scales as the radius to the power of 6 [31]. Optical sorting forces in this regime have a strong size dependence. This relationship has been exploited in sorting applications in sub-wavelength fibre [32], evanescent fields [33] and microfluidic environments [34]. Given particles of equal size, and equal index of refraction (or plasmonic resonance) each of these methods would be unable to distinguish particles based on optical brightness. To overcome the strong size-dependent effect of optical forces, our mechanism applies counter propagating lasers to cancel the size dependent effect of the scattering forces, enabling a new more subtle force to emerge. The optical theory supporting our mechanism is outlined in section 2.3.

2.3 Optical Theory

The sorting mechanism proposed by our project uses near resonant, atomic scattering forces to sort NDs based on defect density.

2.3.1 Estimation of Scattering Force

Scattering forces cause a net movement in the direction of laser propagation due to the directed absorption and scattering of photons. Figure 2.1 represents the free body diagram of the forces that are associated with photon interactions with small dielectric particles (when particle radius is smaller than wavelength). The directed absorption and isotropic emission of photons push the particles in the direction of propagation.

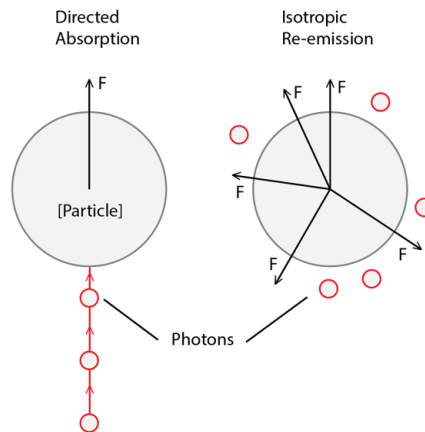


Figure 2.2: The left particle shows the effect of directed absorption; the particle experiences an upward force when photons are absorbed from below. The right particle shows the effect of isotropic re-emissions, photons are emitted in all directions causing no net force over time.

The scattering force $\mathbf{F}_{scat}(\mathbf{r})$ acting on a small dielectric particle is given by equation 2.1 [35], when the particle radius is smaller than the illuminating wavelength ($a \ll \lambda$), where σ is the particles scattering cross section, \mathbf{r} is the particle position relative to the focus of the laser, $\mathbf{E}_0(\mathbf{r})$ is the position dependent electric field strength and $\phi(\mathbf{r})$ is the position dependent phase of the field.

$$\mathbf{F}_{scat}(\mathbf{r}) = \sigma \frac{\mathbf{E}_0^2(\mathbf{r})}{2} \nabla \phi(\mathbf{r}). \quad (2.1)$$

If we consider a travelling plane wave,

$$\mathcal{E}(\mathbf{r}, t) = \frac{\mathbf{E}_0}{2} e^{i\mathbf{k} \cdot \mathbf{r}} e^{-i\omega t}, \quad (2.2)$$

with constant amplitude E_0 , optical frequency ω and wave-vector \mathbf{k} , where the magnitude of $|\mathbf{k}| = \omega/c$. The scattering force is then given by scattering cross section and position dependent intensity.

$$\mathbf{F}_{scat}(\mathbf{r}) = \sigma \frac{\mathbf{E}_0^2(\mathbf{r})}{2} \nabla(\mathbf{k} \cdot \mathbf{r}) = \sigma \frac{\mathbf{E}_0^2(\mathbf{r})}{2} \mathbf{k} = \sigma \frac{I(\mathbf{r})}{2} \mathbf{k}. \quad (2.3)$$

This force acts in the direction of propagation \mathbf{k} . The strength of the force increases linearly with laser intensity and the strength of the scattering cross section. The scattering cross section σ_{bulk} for a small dielectric particle ($a \ll \lambda$) in an aqueous medium is given by,

$$\sigma_{bulk} = a^6 \frac{8n_m}{3c} \left(\frac{2\pi\omega}{c} \right)^4 \left(\frac{m^2 - 1}{m^2 + 2} \right), \quad (2.4)$$

where a is the particle radius, n_m is the refractive index of the medium, ω is the frequency of the laser, $m = n_p/n_m$ where n_p is the refractive index of the particle [36]. From this definition we can see that the bulk scattering cross section changes slowly with laser frequency.

The colour centres in FNDs act as a 2- level system, the scattering cross section for the defects (σ_{atomic}) is given by [35],

$$\sigma_{atomic} = \frac{2d^2}{3\hbar\gamma} \left[\frac{1}{1 + \frac{\Delta^2}{\gamma^2} + \frac{\Omega^2}{\Gamma\gamma}} \right], \quad (2.5)$$

where, d is the dipole moment of the transition, Γ is the transition line width, Δ is the detuning ($\Delta = \omega - \omega_0$), ω is the laser frequency, ω_0 is the transition frequency, Ω is the Rabi angular frequency, \hbar is the reduced planck constant and γ denotes the total line width of the atomic transition and is defined as $\gamma = \Gamma/2 + \gamma_c$ where Γ is the homogeneous term (radiative and non-radiative decay rates) and γ_c the inhomogeneous term accounting for dephasing effects [35]. In comparison to the bulk scattering cross section, the forces on the atomic transition exhibit a strong resonance about the transition frequency. The scattering force is at a maximum when $\omega = \omega_0$ and becomes negligible for large detunings and as a result is highly sensitive to laser frequency. Doped NDs (containing colour centres) have both the bulk and atomic scattering cross sections, where the NDs transition frequency (ω_0) depends on the particular colour centre.

In a system containing both bulk and atomic scattering cross sections, such as NDs containing many N colour centres, the total radiation pressure force on the object is associated with both scattering cross sections and is then given by,

$$\mathbf{F}_{rad} = (N\sigma_{atomic} + \sigma_{bulk}) \frac{\mathbf{I}(r)}{2} \mathbf{k}. \quad (2.6)$$

We can now understand the principal of the sorting mechanism by looking at equation 2.6. By using two counter propagating laser beams with different frequencies we can balance out the force on the bulk object while applying an atomic scattering force with the near resonant laser. **This force will only push the particles that have a high density of embedded defects, sorting them from the particles that experience little or no atomic radiation pressure force.**

2.3.2 Sorting Mechanism

The proposed optical system applies a laser with a detuned frequency (ω_1) and a counter propagating laser that applies a laser with a near resonant frequency (ω_2). The total net force on the ND is then given by,

$$\begin{aligned} \mathbf{F}_{net} &= \mathbf{F}_{rad(\omega_2)} - \mathbf{F}_{rad(\omega_1)} \\ &= (N\sigma_{atomic(\omega_2)} + \sigma_{bulk(\omega_2)}) \frac{\mathbf{I}_2(r)}{2} - (N\sigma_{atomic(\omega_1)} + \sigma_{bulk(\omega_1)}) \frac{\mathbf{I}_1(r)}{2}. \end{aligned} \quad (2.7)$$

The detuned scattering force ($F_{rad(\omega_1)}$) impacts the NDs with an effect that only impacts the bulk scattering cross section of the ND (σ_{bulk}). The force does not interact with the atomic scattering cross section,

$$\sigma_{atomic(\omega_1)} = 0. \quad (2.8)$$

The near resonant scattering force ($F_{rad(\omega_2)}$) is set at an intensity value that removes the size dependent effect of the first laser by impacting the bulk scattering cross section of the ND (σ_{bulk}) with an equal intensity. This value is given by,

$$\mathbf{I}_2(r) = \frac{\mathbf{I}_1(r)\sigma_{bulk(\omega_2)}}{\sigma_{bulk(\omega_1)}}. \quad (2.9)$$

The near resonant scattering force also applies a force to the NDs atomic scattering cross section (σ_{atomic}), where σ_{atomic} is proportional to the defect density of each ND. This result is a defect dependent force in the direction of the near resonant lasers propagation. The setup of this system is represented in figure 2.3 and the net force of the two lasers is calculated using,

$$F_{net} = N\sigma_{atomic(\omega_2)} \frac{I_2(r)}{2}. \quad (2.10)$$

The resulting force is proportional to the number of defects, atomic scattering cross section and the intensity distribution.

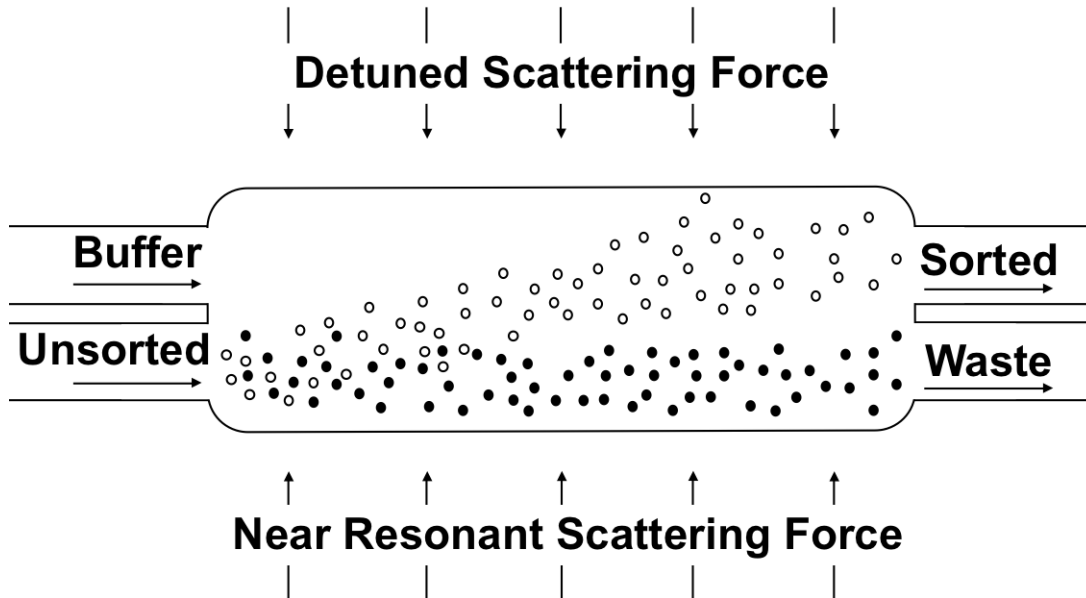


Figure 2.3: Illustrates the effect of the sorting mechanism on 2 particles of different defect density inside the separation channel. \circ are bright NDs (high defect density) and \bullet are dark NDs (zero defect density). The unsorted solution of \circ and \bullet flows from the unsorted feeder with a buffer (water) flowing from the buffer feeder. The NDs move across the separation channel experiencing the 2 scattering forces. The setup shifts the brighter NDs towards the sorted collection feeder while the darker NDs do not shift and are collected at the waste feeder.

2.3.3 Cooperative Effects

Clarice D. Aiello's "Working together" article in Nature Physics News and Views states that "It has been known since Dicke's paper on super-radiance [37] that cooperative effects arise when spectrally indistinguishable two-level systems are near-resonantly excited, while confined to length scales much shorter than their transition wavelengths. Intuitively, any excitation photon must be 'shared' since its wavelength is much larger than the mean distance between the spatially indistinguishable emitters. Alternatively, one can depict the emitters working as a giant, collective dipolar antenna, radiating together in phase with the driving field, and thereby exchanging excitations among themselves" [38].

The cooperative effect in NDs was investigated by Juan et al. [39], and their results suggest that illumination of a ND at the zero-phonon line transition increased the holding strength of the optical trap. The papers authors attribute a 10% increase in optical trap strength at the transition line to the density of defects inside the NDs (the size of the cooperative effect increases as the number of defects increase). This result is significant to our project as cooperative effects could similarly improve the performance of our label-free optical sorting mechanism by increasing the effect of the atomic scattering force for particles with a higher density of defects (brighter NDs).

2.4 Microfluidic Engineering

2.4.1 Background

Microfluidic devices typically exhibit a laminar flow that is suited to the observation and manipulation of a suspended sample of particles. This project will exploit these characteristics to create an optofluidic chip for ND sorting. The key feature of the design is optical accessibility through the base of the channel and the capability to transmit high powered lasers into the microfluidic channel orthogonally to the base.

Generally, the microscale channel benefits researchers with a reduction in the time for analysis, device costs and requisite sample sizes [40]. This field has experienced massive developments as bio based innovators continue to work on both lab-on-a-chip (LOC) and point of care systems. LOC systems are capable of completing complex laboratory experiments with functions that transport, prepare, analyse, detect and separate mediums inside the channels of a microfluidic device [41]. Microfluidic devices are projected as a revolutionary product in health services as diagnostic services use point of care systems to screen bodily fluids [42]. This section will focus on the forefront of microfluidic applications before exploring possible methods of fabrication.

The early development of microfluidic devices worked on the scaling of macroscale assays into a smaller channel environment. Recent developments have worked on devices that apply diagnostics, rapid assays of bio fluids, and drug discovery processes [43]. Microfluidic based diagnostics have dominated diagnostic services since the development of the glucometer and home pregnancy tests. The field has continued to develop towards point of care diagnostics that seek to process a patient's sample in real time. Diagnostic research has continued to reduce the costs of microfluidic production with a shift towards plastic and paper based systems [42]. Single cell analysis and detection is a major pathway for microfluidic devices. For example, systems have been designed to target cancer cells by selectively capturing, manipulating and identifying the cells [44]. Droplet based single cell analysis is viewed as a possible solution to throughput considerations as the droplet enables the isolation and rapid manipulation of rare cells in heterogeneous samples [45]. Microfluidics enables high volume testing for drug discovery applications due to its small size, parallelisability and controlled observation window [46].

2.4.2 Fabrication Processes

Our optofluidic chip requires a smooth sidewall to enable laser propagation inside the channel. This led to the consideration of a wide scope of potential fabrication methods as we identify the surface roughness associated with the vertical sidewalls of each process. This section will review photolithographic, novel methods, ablation processes, etching and micro-moulding techniques to establish a viable fabrication method.

Fabrication methods are often dictated by the material that will create the device. The field developed from microelectromechanical system (MEMS) technologies, creating photolithographic structures on silicon substrates [40]. The opacity of silicon substrates and the expensive processing requirements created a demand for glass based devices, as these designs benefited from an inherent transparency, chemical and thermal resistance. The limitation of using a glass device is that fabrication methods require expensive and specialised facilities. The field has developed towards Polydimethylsiloxane (PDMS) based optical devices that produce cheap device with nanometre resolution [47].

Traditional Methods

Traditional fabrication of microfluidics is a silicon based process that requires photolithography to produce minute structures on a silicon substrate. The process starts with the preparation of the substrate, this step aids adhesion between the substrate and structures. A thin photoresist is applied to the substrate by a spin coater. This resist is selectively exposed to UV radiation through a photomask, which causes the resist to create structures that appear after a development or etching step [41]. Photolithography processes range from minutes to hours, the substrates and photoresist are expensive and the process requires an ultra-clean environment that is designed for the housing of MEMS fabrication equipment. The opaque substrate does not make the product of this process immediately applicable for our project however, it could be used to cast a mould using soft lithography [48].

Soft lithography is commonly used in conjunction with photolithography as it can produce multiple polymer based devices from a single photolithographic plug. These devices are tailored to research applications as they are cheap and quick to fabricate using PDMS material to cast a mould of a structure. Although PDMS based devices exhibit a range of beneficial characteristics the devices suffer from physical and chemical instabilities [49].

Novel Methods

In opposition to the traditional photolithographic methods, novel methods are being developed to create cheap and disposable devices out of readily available plastics and papers. Diagnostic devices are being fabricated using paper and hydrophobic treatments, to create fluidic channels using the wicking effect of paper [43]. Laser printers and lasers cutters are also facing innovative applications as stacked layers of laser cut plastic films are bonded using the printer's ink, enabling the rapid prototyping of microfluidic devices. These methods are novel but inapplicable to our application due to their opacity [48]. Femtosecond lasers have been used for the processing of minute etchings as the laser can accurately ablate a glass surface using a three dimensional, numerical control system. The limitation of this fabrication is that it produces the channels serially and requires extended operation (10's to 100's of minutes) of costly laser technologies [49].

Specialised Methods

Deep Reactive Ion Etching (DRIE) is a method that is often used to produce cavities with a high aspect ratio in glass pieces. The Bosch process of passivation and etching creates vertical sidewall with minute scalloping perpendicular to the wall height. The combination of a DRIE with a potassium hydroxide polish produces a sidewall with a surface roughness close to 50nm. We believe that this process of fabrication is the most promising for our application [50].

2.5 Previous Work

Last year during an Undergraduate Honours thesis [1] we developed a device with a single side access (the optical window was positioned in parallel with the separation channel wall). The device was fabricated using photolithography and soft lithography to produce a PDMS device on a glass base. We placed the fabricated device in the path of a near infrared (NIR) laser in an attempt to observe the effect of a scattering force on a nanoparticle inside the channel [1]. The setup was unable to observe an effect.

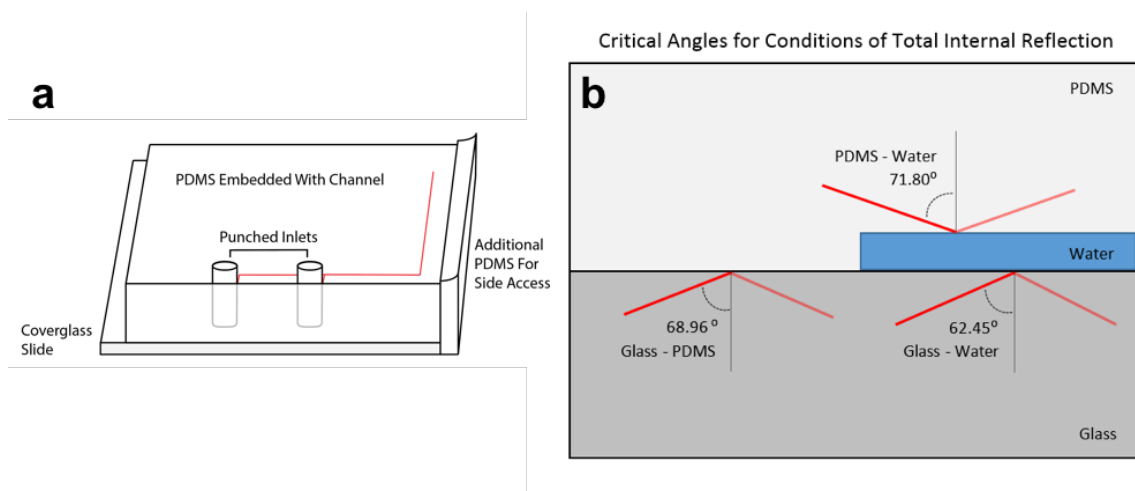


Figure 2.4: Design of the PDMS device that was previously used, features PDMS and an offset channel (a). Conditions inside the channel that caused Total Internal Reflection (b) [1].

We believe that the limitations of the previous experiment included the design of the device and the configuration of the optical path. The device required the light to enter through the side of the channel as the material selection created the conditions for total internal reflection. The channel had the lowest refractive index reflecting incident beams on the top and bottom of the channel. The optical configuration that directed the laser into the 0.1 mm deep channel used a mirror that was mounted 300 mm from the device, this setup limited our ability to determine the laser position relative to the channel. With this device and optical configuration we were unable to distinguish where the waist of the laser was relative to the channel.

2.6 Chapter Summary

This background and literature review contextualises the project to highlight the novelty and associated considerations. The section on FNDs was used to identify the demand that we believe exists for our sorting mechanism and product. The sorting methods and optical theory section highlights potential methods for the mechanism. The fabrication section and previous work outline considerations that we used to direct this year's work.

Microfluidic Fabrication

3.1 Problem Definition

The meticulous design and fabrication of the microfluidic environment was critical to the success of this project's small sorting force. To observe the effect of the sorting, the fabrication needed to create a device where the channel width could be observed and the flow of the particles could be controlled without inhibiting the effectiveness of the sorting mechanism. The fabrication needed to ensure:

- A laminar flow between the input and output ports.
- Observability of the entire channel.
- Separation of the sorted solution from the waste at the collection ports.
- An input port to introduce the unsorted solution and a second input for the buffer.
- An output port to collect the sorted solution and a second output for the waste.
- Effective laser coupling into the channel from both sides.

The following chapter describes the design of the channel and the processes of fabrication, before comparing the optical properties of the different fabrications sidewalls.

3.2 Design Description

Our fabrication process started with the design of a photomask using L-edit software. The design of the mask is illustrated at the top of figure 3.1.

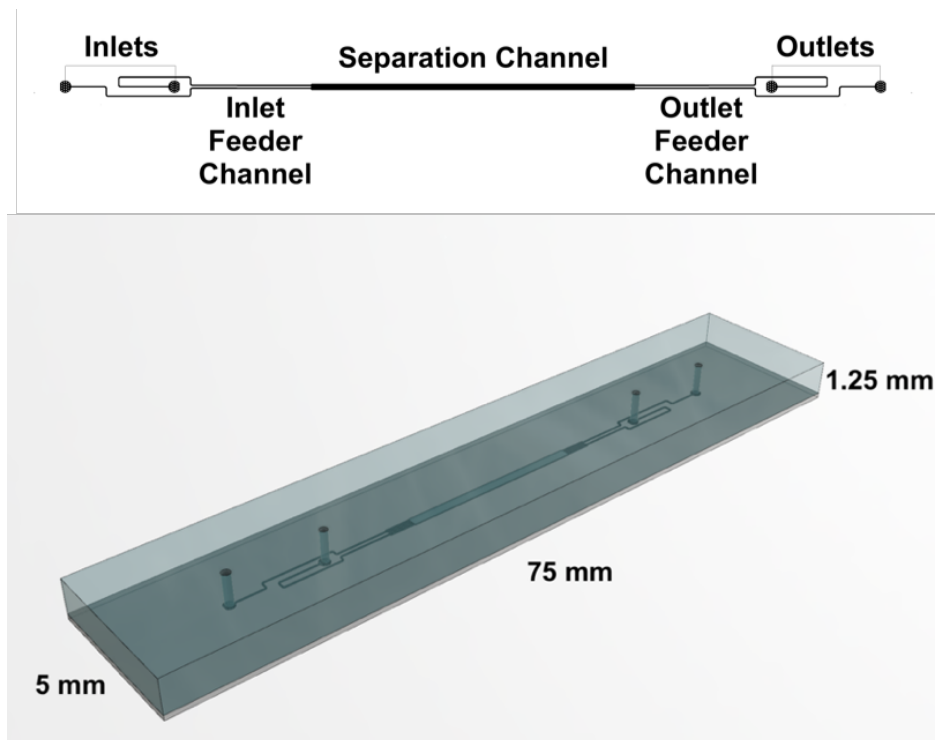


Figure 3.1: Layout of the microfluidic channel that we designed for the sorting of nanodiamonds (top). Dimensions of the fabricated device that was embedded with the designed channel (bottom).

The term channel in this document refers to the complete geometry of the microfluidic channel from figure 3.1 and the term device refers to the microfluidic device that encompasses the channel (figure 3.2). The channel features a separation channel, feeder channels and multiple ports. The inlet ports introduce the solution to the channel and the feeders transport the fluid to the separation channel. The separation channel is the active environment of the sorting mechanism. The feeder channels then transport the unsorted and sorted solutions to the outlets for collection. The linear layout of the design reduced the overall width of the channel, decreasing the amount of material that the laser had to pass through to reach the sidewall of the separation channel.

The dimensions for the separation channel, feeder channels and ports were developed with consideration of existing microfluidic devices and standards. It is a standard to map the ports of a microfluidic chuck to a 9mm grid. Our ports had a 1 mm diameter that featured a grid of 40 μm pillars, these pillars were designed to filter larger particles, to prevent blockages from occurring inside the feeder channels. The feeder channels had a width of 100 μm and a length of 15 mm from channel to port. All of the feeder channels had an equivalent length that ensured that the flow velocity was balanced. The feeder channels were reshaped during the fabrication of the photomasks, to accommodate variations in the overall width of the separation channel (0.5 mm, 1 mm, and 1.5 mm). The bright-field photomask in figure 3.2 is the design that was used to fabricate a collection of microfluidic devices with a varying channel width. Photo sciences inc. fabricated both polarities of photomask with additional dicing lines, grinding marks, identification tags and scale bars.

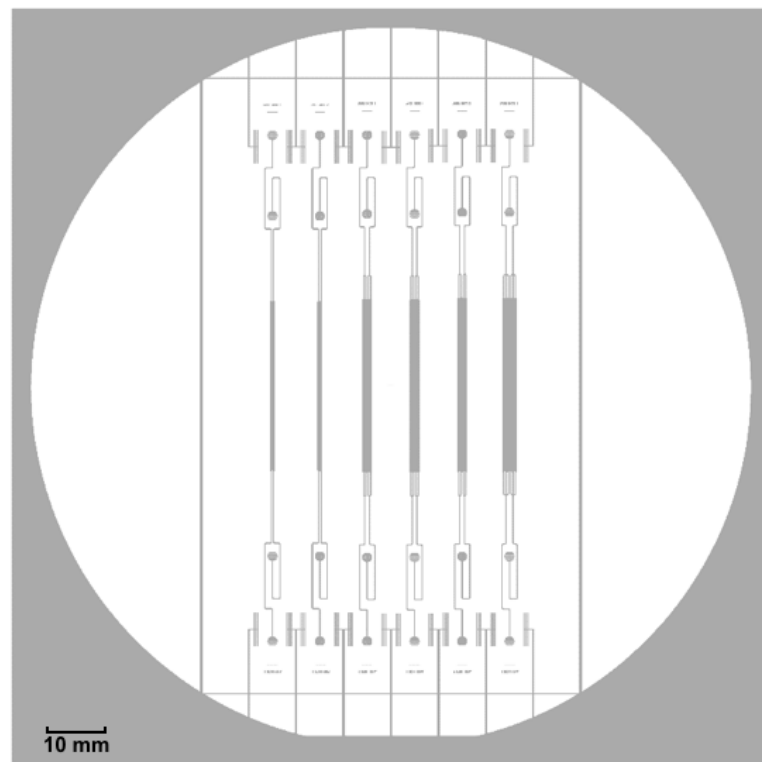


Figure 3.2: Design of the bright field photomask that was used during the DRIE based process. The dark field photomask (opposite polarity) was used during the process of photolithography.

3.3 Processes of Microfluidic Fabrication

We pursued three methods of fabrication to investigate each processes performance and associated costs. The fabrications increased in cost from PDMS based devices, and laser etched Borofloat33 (BF33), to Fused Silica devices that were Deep Reactive Ion Etched (DRIE). This section provides an introduction to the underlying technology and procedure of each fabrication method.

3.3.1 PDMS Moulded Devices

Technology Introduction

Photolithography and soft lithography are often combined to produce PDMS based devices. The process of photolithography uses photomasks and photo sensitive coatings to produce a desired plug shape that is used during soft lithography to mould the PDMS [51]. The following process was completed on the Macquarie University Campus using the physics and engineering clean room facility. The process of photolithography follows the procedure outlined in the datasheet for GM1070 SU-8 (Gersteltec) [52].

Procedure

Photolithography - This process used a negative photoresist (GM1070 SU-8) and a 3 inch silicon wafer. An oxygen based plasma system cleaned the organic material from the surface of the silicon substrate. The wafer was dehydrated on a 120 ° C hotplate for 5 minutes. A spin coater applied a 100 µm layer of SU-8 GM1070 photoresist to the silicon wafer (this height determines the depth of the device). The spin coater uses centripetal forces to evenly distribute the resist with the spin rate determining the thickness. The coated wafer was heated on a ramping hotplate to release the solvents from the photoresist. The coated wafer was then placed in a UV exposure system to selectively expose the substrate to UV radiation. The dark field photomask was used to apply UV radiation in the shape of the channel, this exposure hardened the exposed resist and an additional post bake on the ramping hotplate further increased the strength of the hardened SU-8 structures. The silicon substrate and SU-8 structures were developed in a bath of SU-8 developer. The developed plug was rinsed with isopropanol and dried using a nitrogen gun.

Soft lithography - The PDMS was produced using Sylgard 184 base and curing agent, the two parts were measured, combined and then degassed in a disposable weighing boat. The degassed mixture was poured over the photolithographic plug and an additional clean wafer. Both wafers were placed in an oven at 65 ° C to set the PDMS. After the PDMS had set, it was peeled from the plugs and applied to a clean acrylic sheet. The ports were then punched through the moulded PDMS using a biopsy punch. The bonding surfaces of both peels were then prepared for a fusion bond using the oxygen plasma system. The bond was formed by placing the bonding surfaces in contact. The PDMS devices were cut to size using a utility knife and rule. To increase the devices orthogonal optical accessibility, the PDMS devices were placed on their sides above a glass slide and additional PDMS filled the gap between the glass and the side of the device.

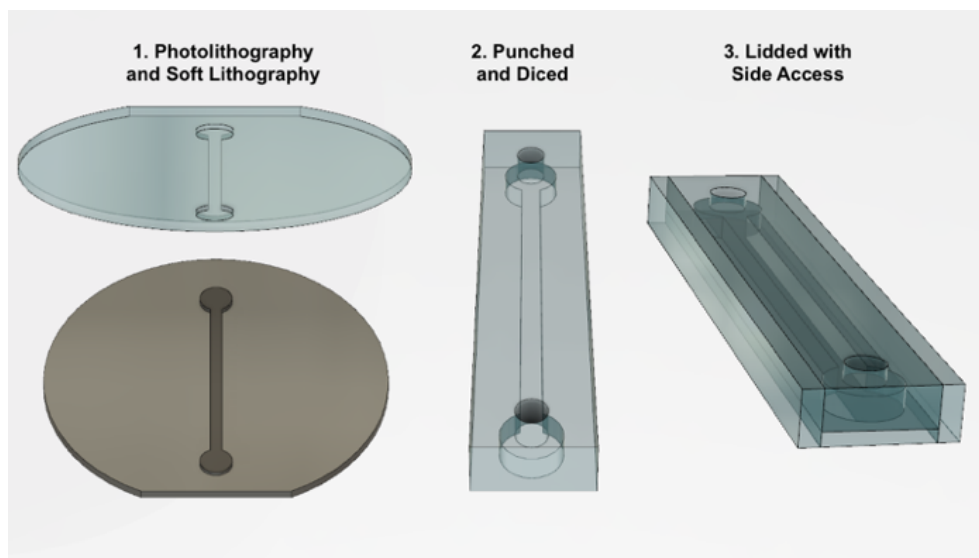


Figure 3.3: Schematic of the process used to produce the PDMS based devices. The channel design has been simplified in this representation, as the actual channel shape is the same for all of the fabrications (top of figure 3.1). **1.** Photolithography produced the shape of the channel on a wafer (brown) and Soft lithography moulded the PDMS to the shape of the wafer plug (light blue). **2.** The moulded PDMS was placed on an acrylic sheet, to punch the ports and dice the piece. **3.** The piece was lidded with an additional piece of bonded PDMS before PDMS windows were applied to the sides of the device.

3.3.2 Laser Etched Borofloat33

Technology Introduction

Optofab, the Laser Micromachining Facility at Macquarie University used a Picosecond laser to etch the surface of a Borfloat33 (BF33) piece. The laser used a process of ablation to etch the design into the material. The process uses the absorption of a rapidly pulsing, tightly focused laser to remove material as its temperature increases to the evaporation point [53].

Procedure

The surface of the BF33 pieces was prepared for etching with a protective layer of AZ 1518. The laser technician used a computer aided design of the channel to define the path of the laser. The etch rate and etch depth were determined as functions of laser power and number of passes to produce an 80 μm deep channel. To protect the etched surface, layers of SU8 and tape were applied to prevent damage from occurring as the ports were drilled. The position of the ports was marked on the tape and the inlets/ outlets were tapped using a Danville Materials Microetcher, this microetcher used a fine sand to drill a well from the top surface of the BF33 to the ports. After the ports were formed, the protective tape and photoresist were removed from the piece as it cleaned in a bath of acetone and isopropanol. The clean channels were sent to ANFF at the University of South Australia to be lidded and annealed with a 150 μm BF33 wafer. The lidded device was diced using a wet, disc saw.

3.3.3 Deep Reactive Ion Etched Glass

Technology Introduction

The Bosch process of Deep Reactive Ion Etching (DRIE) produced the shape of the microfluidic channel in a Fused Silica Wafer (Hoya Inc.). The Bosch process alternates between passivation and etch steps, to remove material from the exposed surfaces of the wafer. The passivation step applies a protective polymer before the etch step uses a directional bombardment of ions to penetrate the protective layer from above (figure 3.6).

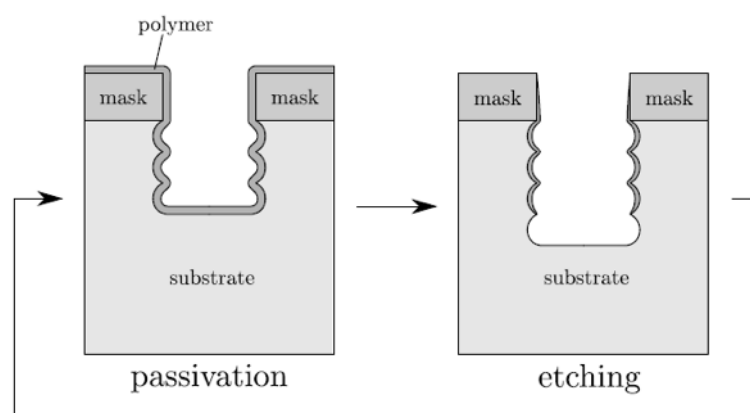


Figure 3.4: Representation of the iterative nature of the Bosch Process of DRIE [54]. The location of the etch is often defined by an etch mask that is applied to the substrate by a process of photolithography, this step ensures that the etch only removes material from the exposed regions of the substrate (defines the shape of the etch).

Procedure

The DRIE process of fabrication was completed in collaboration with the ANFF facility at the University of South Australia. The staff at ANFF cleaned the fused silica wafer in a plasma cleaner before a negative etch mask was applied by photolithography. This mask consisted of a protective layer of SU8 photoresist that was coated in layers of chrome and gold. The iterative Bosch process of DRIE was then used to remove 60 μm of the quartz material from the non-protected regions of the wafer. After the surface had been etched it was returned to Macquarie University and additional photoresist and tape were applied to protect the surface from damage as the Microetcher drilled the ports. The ports were marked and drilled before the wafer was cleaned in a bath of acetone and isopropanol. To remove the protective layer

of SU-8 / chrome / gold the piece was soaked in chrome etchant and Remover PG baths. The etched surface of the wafer and a 110 μm wafer were prepared for bonding with a piranha clean and ammonia hydroxide bath. The two surfaces were dried and pressed together on a flat surface to form a temporary bond between the two pieces. These bonded pieces were then annealed in an oven at 1000 ° C for 24 hours. The lidded piece was then returned to the University of South Australia facility for dicing.

3.4 Device Overview

The devices were designed with the same channel geometry and a width of 5 mm. The PDMS devices were soft and flexible while the two glass devices were hard and brittle.



Figure 3.5: The three devices that were created by different fabrication processes. The ports of all three devices are visible but the channel visibility varies with surface roughness. The inability to see the channels of the PDMS and DRIE devices indicates a smoother surface. The channel of the laser etched piece appears frosted due to the rough finish produced by the laser etching process.

3.5 Scanning Electron Microscopy

The optical accessibility of each fabrication was a major consideration during the design of the microfluidic environment. Optical accessibility benefits from a surface roughness that is smaller than the illuminating wavelength. For our system, both the exterior and interior interfaces need to be smooth to ensure effective optical coupling. To gain an indication of the surface roughness of the sidewalls, a scanning electron microscope (SEM) imaged walls of each device type.

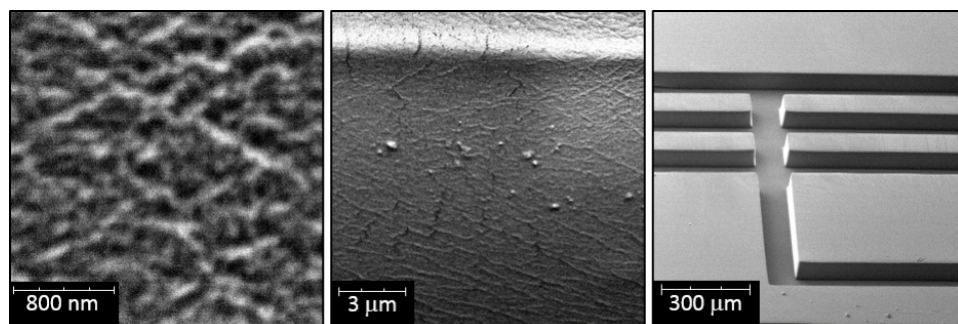


Figure 3.6: SEM images of the sidewall created by a PDMS peel

The surface roughness of the PDMS peel was relatively similar across the wall, small cracks occurred due to the sheering removal of the peel and small impurities also stuck to the sidewall due to the tacky nature of the material. Despite these cracks and impurities, the average feature size in this image was 200 nm.

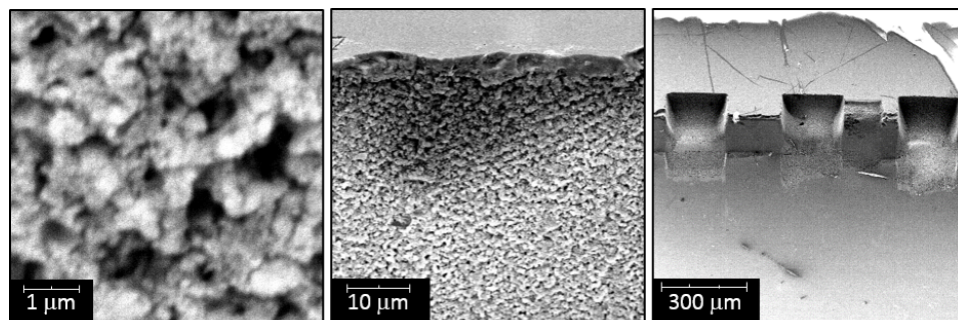


Figure 3.7: SEM images of the sidewall that was laser etched BF33

The surface of the laser etched material featured a carpet like texture that occurred due to the raised temperature of the ablation process. The surface was populated by 500 nm sized globs of previously molten glass.

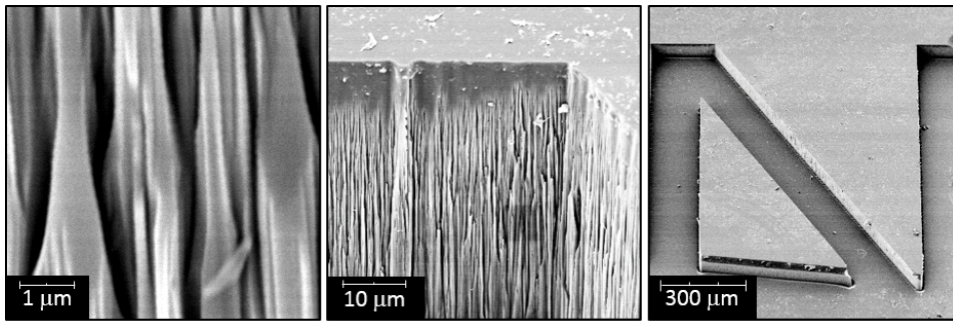


Figure 3.8: SEM images of the sidewall that was DRIE into fused silica [55].

The DRIE sidewall featured a grass artefact that appeared at a depth of 10 μm . Grassing arises from an etch resistant patch preventing the etches progress, this resistance path propagated into 1 μm cones (at a depth of 30 μm).

3.6 Discussion

The three fabrications accurately produced devices with an embedded channel. Each method has associated costs. A set of 6 PDMS devices required 12 hours for fabrication at a cost of \$600. The resulting devices were elastic, adaptable and optically transparent. The soft nature of the PDMS devices decreases the predictability of the channel, as the roof of the channel can droop [56] and the composition of PDMS accepts dyes (such as rhodamine 6G) [57]. The laser etched chips required 3 hours for fabrication at a cost of \$450. The ease of fabrication was offset by the non-linearity of the etch rate, the roughness of the sidewall and the material build up on the top of the surface. The material build-up made the bonding more difficult and led to the outsourcing of the bonding to ANFF at South Australia. The devices that were fabricated using DRIE exhibit a strong bond with a thin lid that is suited to our project. These DRIE devices required two weeks for fabrication at a cost of \$2400 for 12 devices.

A recent patent by Cather Simpson from the Photon Factory focuses on the sex-based sorting of bull sperm. The sorting mechanism uses multiple lasers to sort and orient the sperm as it passes through the channel. Their work initially used micro fabricated devices before targeting off the shelf square capillaries. Their unpublished research believes that optical coupling is increased for these capillaries, as glass redrawing produces a flat surface. Future fabrications could improve the efficiency of the optical coupling using a similar square capillary based design, but the process would require considerations for connection of the feeder channels and ports.

3.7 Chapter Summary

This design chapter investigated different fabrication methods to find an experimental chamber that could be used to sort NDs using multiple lasers. The design requirements defined the devices shape before we fabricated PDMS moulded, laser etched and DRIE devices. The sidewalls of the channels were imaged with an SEM to understand the surface roughness associated with each fabrication.

4

Optical Configuration

4.1 Experiment Introduction

The optical setup was designed to investigate the effect of optical forces on a selection of particles. The variables of the chuck design, optical path, and particle selection were developed with consideration of the projects small sorting force. The primary aim of the experiment was to characterise the effect of the scattering force on particles. Achieving this aim required:

- The observation of diffusing particles within the microfluidic channel,
- Laser propagation inside the channel (to validate the devices' optical accessibility),
- A directional scattering force that impacts the suspended particles.

This chapter reviews the chuck design, particle selection, optical theory and optical configuration that achieved these aims.

4.2 Particle Selection

The size of the scattering force is dependent on the strength of the scattering cross section of the impacted particle (equation 2.3). Our experiments tested two large particles as these particles could be viewed on our microscope setup:

- ND (Lucigem)
- Fluorescent Beads (Polysciences, Inc.)

The bulk ND was produced using HPHT synthesis, the output was processed to clean the graphite off the NDs and sort the sample to a specified particle size [8]. We used Dynamic Light Scattering (DLS) to determine that the sample was mono-dispersive with an average particle radius of 149 nm. The DLS results also showed an aggregation rate at the boundary of good to moderate stability. This rate of aggregation requires an ultrasonic bath every 2 hours. The concentration of the stock was estimated at 0.01 mg/ml. This sample was not processed to increase the defect density (but it has naturally occurring population of NV centres).

The fluorescent beads used are polystyrene-based spheres that are internally dyed with Fluorescein (YG) dye. The particle has a size distribution with an average radius of 250 nm and a concentration of 4×10^{11} particles/ml.



Figure 4.1: The nanomaterial dilutions that were processed in the laser scattering experiment placed in front of the larger stock containers. The bulk ND samples are on the left and the fluorescent bead samples are on the right.

4.3 Chuck Design

The optical setup required the fabrication of an optofluidic chuck that could mount the microfluidic device and supply fluid into its ports. The chuck was designed to mount the device's separation channel in the path of the laser. The chuck's grooves enabled the mounting of the chuck onto the threaded posts, the chuck rested on nuts and the posts were fastened to the breadboard stage. To mount the device, two base plates that featured two fastening holes and two smaller alignment windows sandwiched the device to the chuck using four screws (figure 4.2 b). The chuck was machined to connect the four ports of the device to inlet tubing and a syringe via a flat bottom 1/4 - 28 port and fitting. Flat bottom connectors use a nut and ferrule to seal the fitting, the nose of a flat bottom ferrule is pressed against the nut and the bottom of the port as the fitting is screwed in. Underneath the chuck o-rings sealed the gap between the ports of the device and the chuck.

To ensure that the mounted device could be illuminated the chuck was manufactured from Perspex to allow light to pass through the material. The chuck featured cut outs on the base of both sides, to enable the unobstructed travel of the beam path to the position of the device. One side was completely cut out to allow optical elements to be placed closer to the chuck without interaction between the component and the chuck.

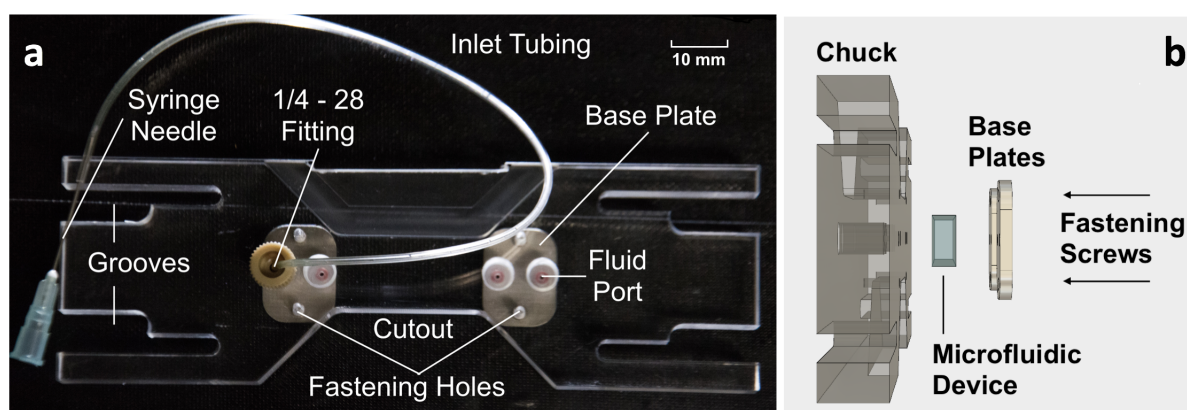


Figure 4.2: Annotated photograph of the left chuck with a microfluidic fitting connecting a syringe needle to a port of the chuck (left). Configuration of chuck, device and base plates that mount the device (right).

4.4 Optical Theory

We used Gaussian beam optic theory to design the optical configuration through calculations of the different beam requirements. In a simplified Gaussian beam the beam spot size $W(z)$ is the radius of the laser profile for a given z , where z defines the axial displacement from the focus of the laser. The beam waist (W_0) is the radius of the beam spot size at the focus of the laser ($z = 0$). The Rayleigh regime (z_R) is the distance from the focus to a point where the beam width increases to $\sqrt{2}W_0$. These Gaussian beam parameters are illustrated in figure 4.3.

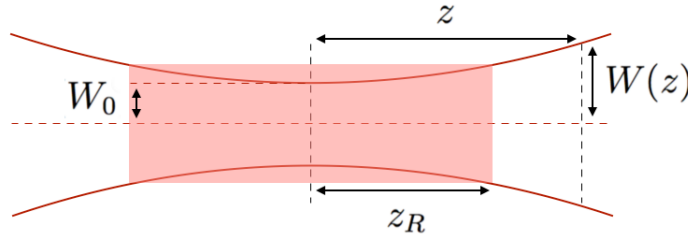


Figure 4.3: 2-Dimensional Representation of Gaussian Beam Parameters. z_R is the Rayleigh regime, $W(z)$ is the beam spot size, z is the displacement from the focus along the path of laser propagation and W_0 is the beam waist.

These parameters can be calculated using two equations,

$$z_R = \frac{\pi(W_0)^2}{\lambda}, \quad \text{and} \quad (4.1)$$

$$W(z) = W_0 \sqrt{1 + \left[\frac{z}{z_R} \right]^2}, \quad \text{where} \quad (4.2)$$

$$\approx W_0 \left(\frac{z}{z_R} \right) \quad \text{when} \quad z \gg z_R.$$

These equations were used to calculate the focal length that was required for a desired beam waist. At the lens ($z = f$) the spot size of the beam is equal to the beam divergence ($W(f) = \mathcal{D}$), where beam divergence (\mathcal{D}) is the angular component of a beams increasing radius and f is the distance from the lens to its focal point. At this point the axial displacement

(z) was significantly larger than the Rayleigh range of the laser and the approximation from equation 4.2 could be used for the focus (f). Substituting \mathcal{D} and f into equation 4.2 yields,

$$\mathcal{D} = W_0 \left(\frac{f}{z_R} \right), \quad \text{using equation (4.1) and rearranging for } f \text{ gives,} \quad (4.3)$$

$$f = \frac{\pi W_0 \mathcal{D}}{\lambda},$$

where λ is the wavelength of the laser. This equation can be solved for a desired beam waist W_0 , as the values for \mathcal{D} and λ are defined by previous optical elements in the beam path and the laser. Using these equations the optical configuration was designed to impact the device with a beam waist that was equal to the channel height of 100 μm .

4.5 Configuration of Optical Elements

4.5.1 Components

The optical setup was designed to direct two lasers into the microfluidic channel from opposite sides of the device. The wavelengths of the laser diode had two distinct values: the green laser ($\lambda = 532 \text{ nm}$) had a near resonant scattering effect (defect density dependent + size dependent) and the near infrared laser ($\lambda = 785 \text{ nm}$) had a detuned scattering effect (size dependent). The setup used a combination of mirrors and lenses to direct and focus the laser into the channel. The scattering from impacted particles produced an image at the focal plane of a microscope objective that was captured on a CCD camera. The optical setup used laser diode controllers, mounted laser diodes, fibre elements, lenses and mirrors to implement this design.

4.5.2 Optical Path

This section reviews the optical path from the laser diode to the camera, featured in figure 4.4. The laser fields were created by mounted diodes, one producing a green emission at a wavelength of 532 nm and the other at 785 nm (near infrared). The lasers were coupled into fibre that was used to translate the laser from the table to the height of the stage. We then collimate the laser out of the fibre (ensuring no beam divergence). The collimated

Gaussian beam allowed for the converging lens to be positioned at any point along the optical path. The setup then used a spherical lens to focus the collimated light to the designed beam waist inside the channel. Two mirrors were used to direct the focus of the laser to a point inside the mounted device, designed to adjust the beam position relative to the channel. The microscope objective was positioned below the optofluidic chuck to capture a magnified image of the channel. This image was focused on a Nikon Digital CCD camera that was computer controlled.

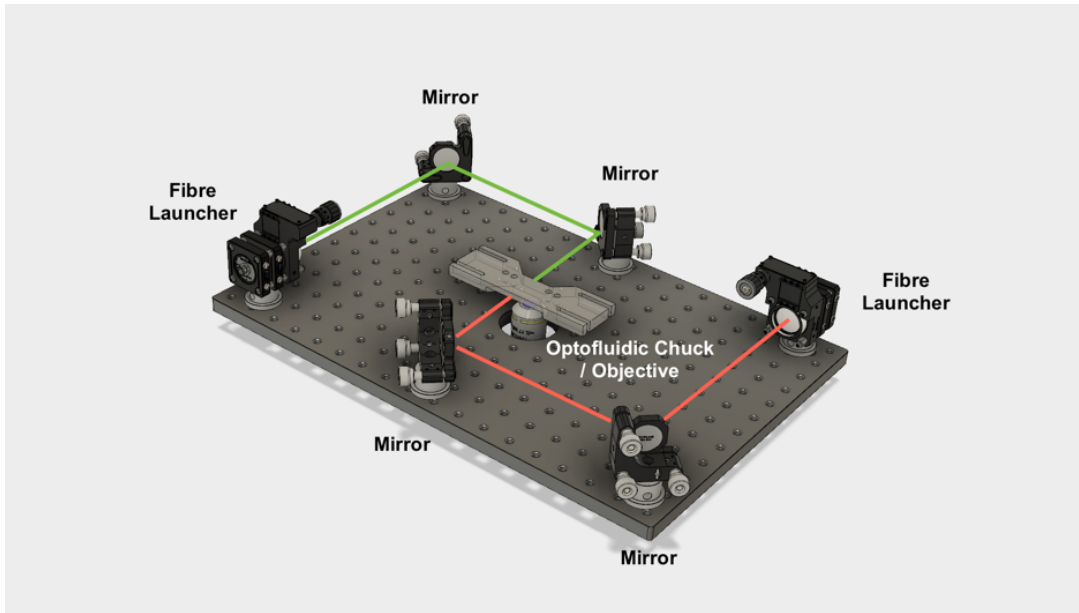


Figure 4.4: Schematic of the optical path on the stage of the optical configuration. The light from the fibre launchers is collimated then focused before reflecting off two mirrors towards the device that is mounted to the base of the chuck. To increase the laser power it is also possible to replace the fibre launchers on the stage with diode mounts or mirrors that can direct the laser in free space.

4.6 Discussion

Revisions were made to improve the performance of the optical and microscope configuration. The green diode was raised to the height of the stage in free space to reduce the losses in laser power that occur while coupling into fibre (approximately 50% of laser power). A lens with a shorter focal length increased the power density of both laser wavelengths by reducing the width of the beam waist from 100 μm to 20 μm .

4.7 Chapter Summary

This optical configuration chapter explained the method and materials that were used to control the laser. This section reviewed the optical requirements and nanomaterials before outlining the design and setup of a system that impacts an optofluidic device with a scattering force.

5

Results

5.1 Hypotheses and Expected Results

The primary aim of this project was to quantify and characterise the scattering force effect. This required the design and fabrication of a microfluidic environment and optical configuration that could enable this quantification. The microfluidic environment needed to entrain the particles in a controlled flow while providing optical access into the channel. The optical configuration needed to impact the particles with a scattering force.

We completed 2 sets of experiments to understand the performance of our setup. The first test investigated the ability of the different microfluidic fabrications to couple laser light into and across the channel. The second set of experiments observed the effect of scattering forces on suspended particles inside the microfluidic channel. While completing these experiments we expected the laser transmission to depend on surface roughness, and for the scattering force effect to depend on particle variations. This chapter reviews the procedures of the optical coupling experiment and the laser scattering force experiment to process the results.

5.2 Optical Coupling Experiment

The aim of the optical coupling experiment was to quantify the amount of light that was transmitted through the sidewalls of different fabrications. The laser power was expected to decrease due to scattering within the medium (attenuation) and at the interfaces between different mediums (refraction and reflection). This experiment varied the test channel conditions and laser colours to test the optical accessibility of the three fabrications.

Procedure

The three devices that were fabricated for this experiment were a moulded PDMS device, a laser etched device and a DRIE device (previously described in chapter 3 and imaged in figure 3.5). The optics were setup to direct the path of the laser through the mounted device to a power meter that was positioned 100 mm from the edge of the mounted device. The laser power was set at 0.1 mW for the green laser and increased to 10 mW for the infrared laser.

The first measurement, recorded a reference for the laser power when the device was removed and the path of the laser was continuous. The following measurements recorded the transmitted laser power after it had travelled through the device. Reference and transmitted measurements were recorded at multiple points along the length of the separation channel before the chuck was flipped and the transmission was measured from the other side. The laser transmission was tested for all three fabrications with different channel environments and laser wavelengths:

- Dry channel environment/ Red laser (DR);
- Dry channel environment/ Green laser (DG);
- Wet channel environment/ Red laser (WR);
- Wet channel environment/ Green laser (WG).

Results

The results of the experiment are summarised in figure 5.1. Wetting the channels improved the transmission under all test conditions. The PDMS devices achieved the highest transmission of red laser power, the DRIE devices performed consistently for both of the wavelengths, and the laser etched devices exhibited the lowest transmission rates. We believe that these experiments show that the sidewall roughness of the fabrications, and the illumination/channel conditions define the laser transmissibility. The coarse finish of the laser etched sidewall prevented the laser from effectively crossing the channel. The PDMS device did not interfere with the longer wavelength of the red laser but limited the green transmission as the size of the imperfections were closer to the wavelength of the green laser. The DRIE device exhibited effective coupling for all of the test conditions, this could be attributed to the larger size of the sidewall defects.

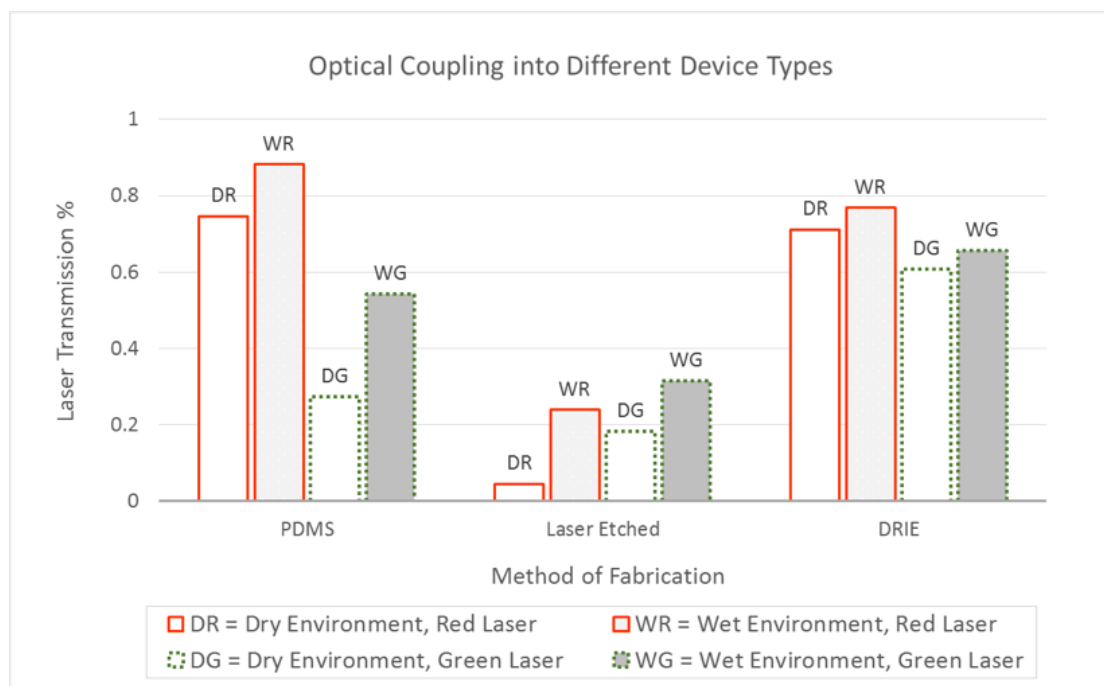


Figure 5.1: Laser transmission for the fabrication types with variations in the channel environment and laser. The wet channels had a higher transmission as the increased refractive index of water reduced losses at the interfaces. The PDMS device had the highest transmission of the red laser but a lower transmission of the green laser. The laser etched device had the lowest transmission rates due to the roughness of the sidewalls. The DRIE device had a relatively constant transmission rate of 70% of laser power across both laser wavelengths.

5.3 Laser Scattering Force Measurement

The aim of this experiment was to establish an understanding of scattering forces (detuned and near-resonant) that would support the sorting mechanism we have proposed. In this thesis we have established an optofluidic environment that enabled the testing of these forces. The typical preparation and procedure for characterising scattering force is outlined below.

Preparation

To observe the scattering force effect the samples were diluted to a trackable concentration. The dilutions were completed in 100x steps to reach a point where the particles movement was distinct and the path could be tracked over consecutive frames. We created 10,000x dilutions of the two stock samples by mixing 0.1 μ l of the stock with 1 ml of deionised water. The diluted sample was prepared for the experiment using a 30-minute ultrasonic bath to scatter the aggregates and disperse the sample.

To prepare the microfluidic elements we pushed 1 ml of ethanol through the microfluidic chuck, tubing and connectors and collected the output in a waste container. These accessories were subsequently flushed with 2 ml of deionised water, and air before use. After the accessories were cleaned a microfluidic device was mounted and similarly flushed with ethanol, water, and air (a syringe removed the waste fluid from the other ports). This experiment used the DRIE devices due to their performance in the optical coupling experiment.

To setup the imaging path the objective was mounted to a z-translation stage and the CMOS camera was connected to the computer by a USB cable. With an image displayed on the computer, the chuck was placed onto its threaded mounting rods with the channel positioned above the objective at the height of the optical path. The exposure and focus of the image were adjusted using the software and z-translation stage respectively. After the image was focused, a 100 μ l sample could be pushed into the channel and the scattering from the particles could be observed through the microscope.

Method

We investigated the effect of scattering forces on bulk NDs and Fluorescein Fluorescent Beads given a fixed laser power. After feeding one of the samples into the channel of the DRIE device, 10 minutes were required to reduce the particle drift. Once the particles were relatively static we traversed the horizontal position of the laser using the adjustment knobs on the mirror mounts. This scanning procedure aimed to locate particles within the vertical beam waist of the illuminating laser. We then record a time-lapse when a particle was inside the beam (scattering) and adjusted the mirrors to compensate for residual flow or diffusion along the channel. This scanning and recording process was repeated for more than a hundred ND particles before the experiment was repeated for the fluorescent bead sample. The time-lapsed image sequences from this experiment were processed with a particle tracker to understand particle behaviour.

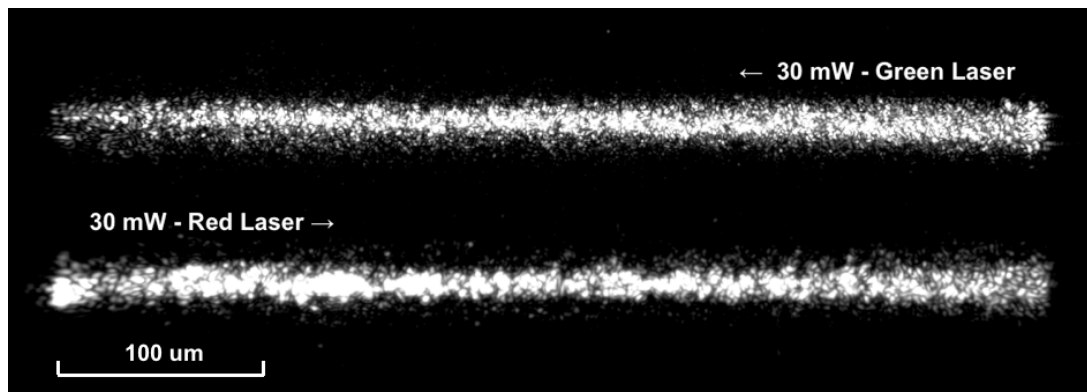


Figure 5.2: Image of the red and green laser crossing the channel. A higher concentration of particles was used to clearly show the path of the laser through the channel. This image was edited to superimpose images of different focuses, we were unable to focus the images of both lasers simultaneously.

Tracking procedure

We used MtrackJ (a manual particle tracking plugin) on the ImageJ software [58] to track the particle trajectories. The plugin recorded the user selected pixel location of the particle in each frame to map the path. The plugin used these trajectories to calculate the frame-to-frame displacement and the relative angle between consecutive points. The recorded trajectories were tabulated in a spreadsheet and processed using Matlab.

To track a bead in figure 5.3, we would click on the location of the particle and track it through the available frames before returning to track another particle.

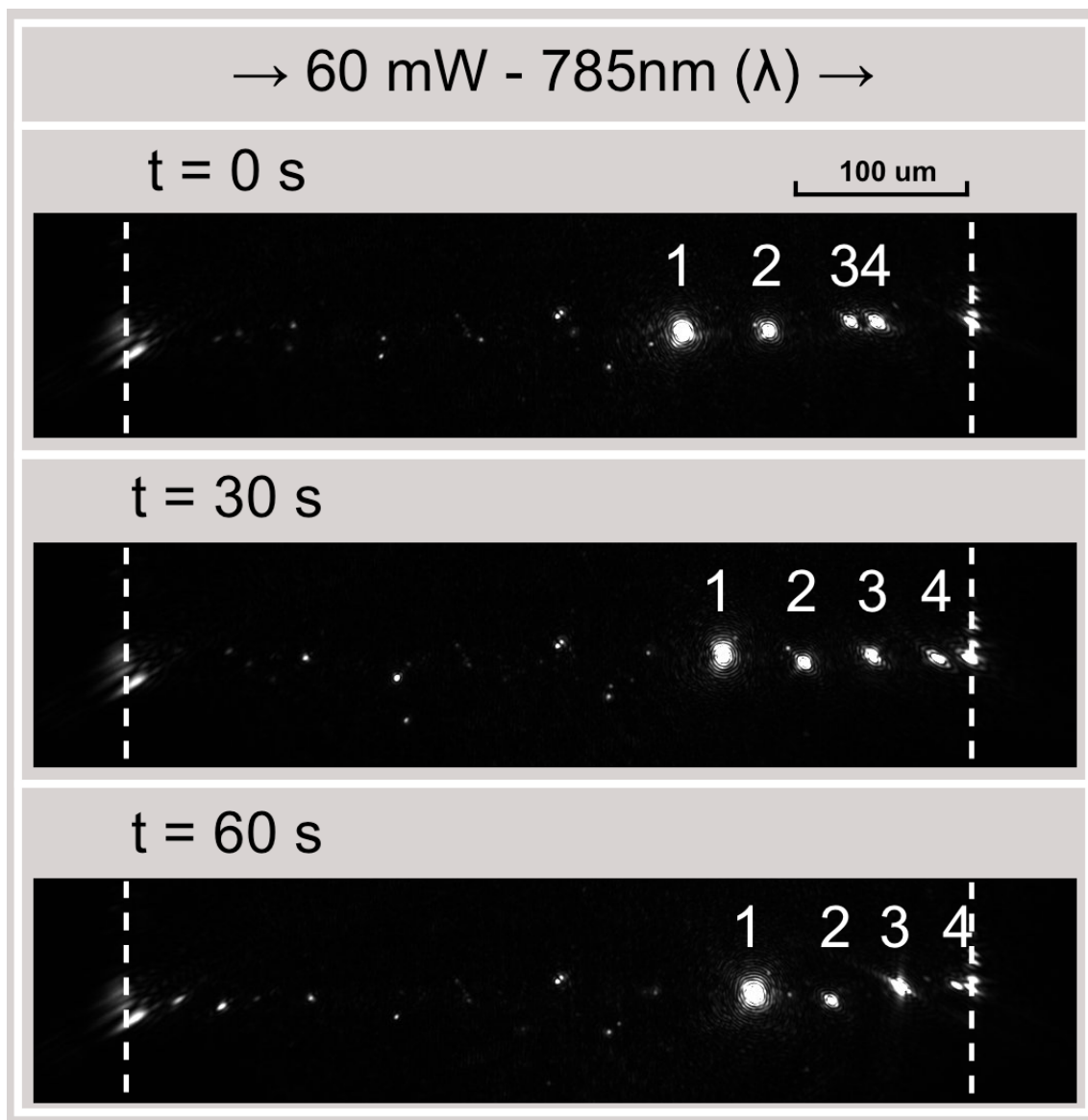


Figure 5.3: Timelapse of four fluorescent beads experiencing a scattering force. The beads were pushed to the right of the image by a 60 mW laser that had a wavelength of 785 nm (red). The channel walls are marked in the images with a broken white line.

5.4 Processing of Tracking Results

5.4.1 Matlab Output

Matlab processed the tracking results, by inputting the spreadsheets as readable arrays. The images in figure 5.4 were created in Matlab. These plots shift the trajectory of each particle to start at a common origin. This figure of overlaid trajectories gave a visual indication of the orientation and scale of each trajectory.

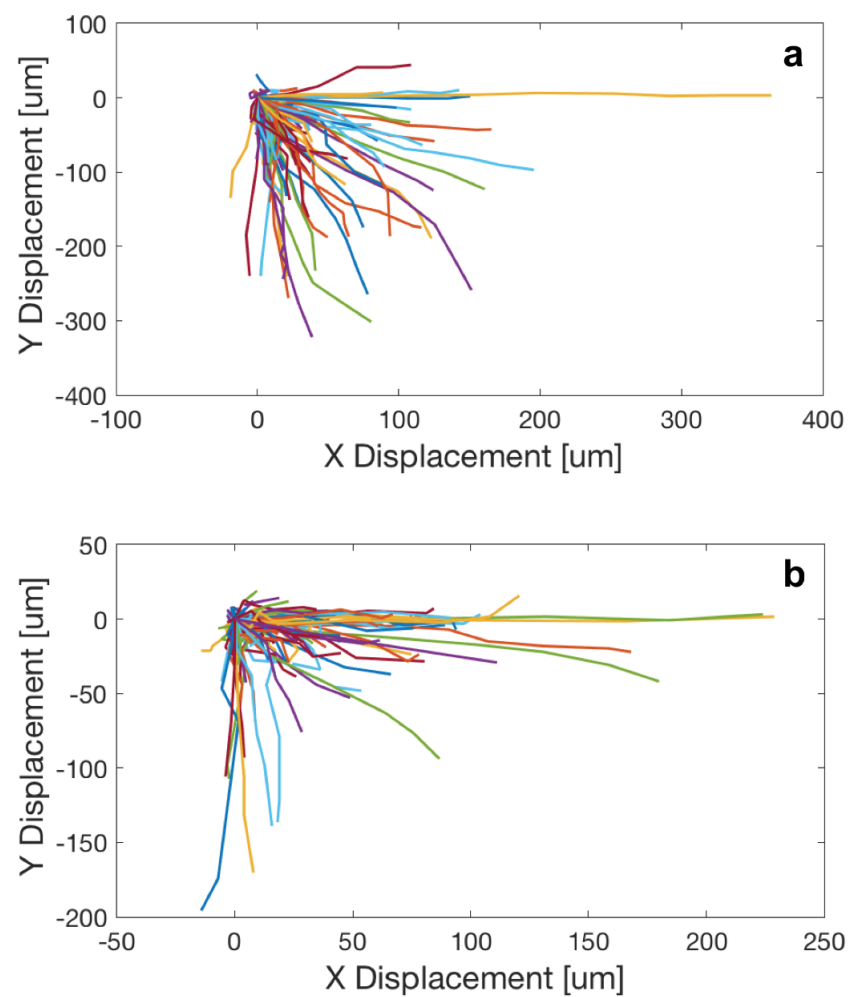


Figure 5.4: Overlaid trajectories from the scattering force experiment using a 60mW laser at 532 nm (λ) on two types of particle, ND (a) and fluorescent bead (b). The overlaid trajectories show the pushing force of the laser to the right (X Displacement) and the effect of flow moving the particles down the channel (Y Displacement).

Figure 5.5 was processed in Matlab using two sets of data for each particle to understand the effect of the scattering force relative to diffusion. The code used the frame rate, displacement per frame and angle of displacement to calculate the axial velocity of the particles for the two data sets. The first data set recorded the particle velocity inside the beam waist (experiencing a scattering force) and the second set recorded the velocity of particles outside the beam waist (diffusing).

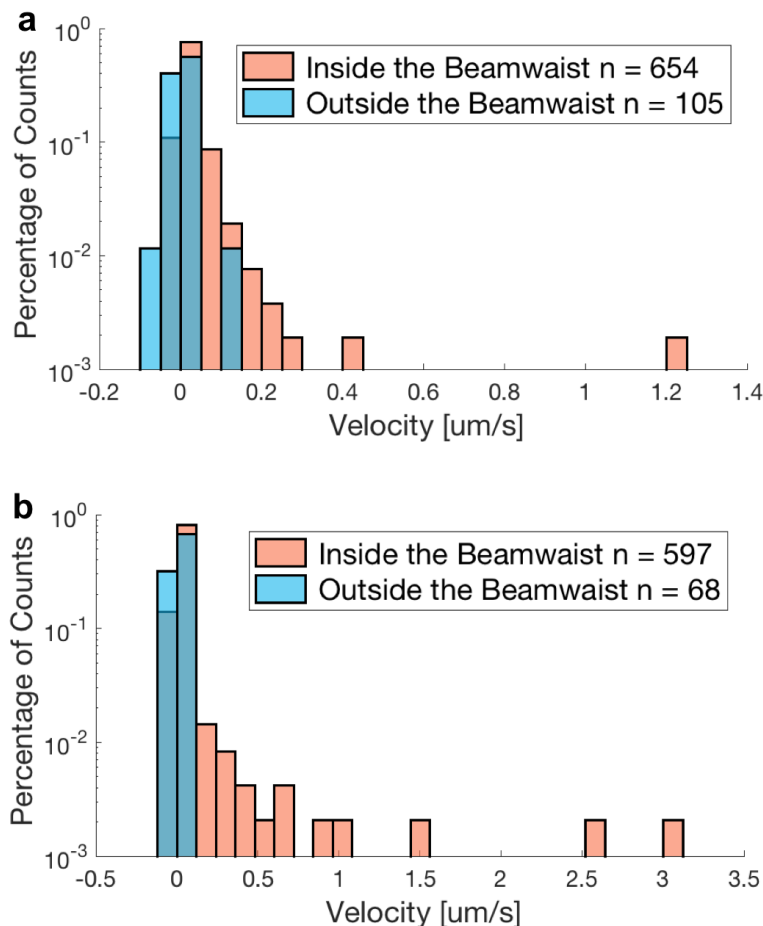


Figure 5.5: The axial (X) velocity of scattering and diffusing particles in a 60mW laser at 532 nm (λ) visualised with normalised histograms on a logarithmic scale. Plot (a) represents ND and (b) represents fluorescent bead, where the blue columns are the particles outside the beam waist (diffusing) and the orange columns are the particles inside the beam waist (scattering). These plots show the positive velocity experienced by the scattering particles while the diffusing particles do not experience a scattering force (approximately no net displacement).

5.4.2 Calculation of Scattering Force

Using the tabulated data and the shape of the histogram we averaged the velocity of the fastest 10% of the particles inside the beam waist (using the assumption that these particles are experiencing a scattering force). The mean scattering velocity for the two particles (v_{ND} , v_{FB}) was used to calculate the size of the scattering force (F_{scat}) experienced by each particle. This calculation used Stokes' Law for the force on a sphere that is moving with velocity in a viscous fluid,

$$F_{scat} = 6\pi\mu a v, \quad (5.1)$$

where μ is the dynamic viscosity of the medium, v is the particle velocity and a is the radius of the sphere. Table 5.1 uses the scattering velocities (v_{ND} , v_{FB}) to calculate the scattering force using equation 5.1, where the dynamic viscosity (μ) of water is 1 mPa.s at 20° C.

Table 5.1: Calculation of the Scattering Force for a given velocity

Particle Type	Nanodiamond	Fluorescent Bead
Radius	149 nm	250 nm
Scattering Velocity	0.129 $\mu\text{m/s}$	0.318 $\mu\text{m/s}$
Scattering Force	0.361 fN	1.498 fN

From table 5.1, the fluorescent beads experienced a scattering force that was more than four times the force experienced by the nanodiamond, this force is related to the increased velocity of the larger particle.

5.4.3 Calculation of Intensity Distribution

The results of the laser coupling experiment were used to calculate the intensity distribution of the laser inside the channel of the DRIE device. The laser power outside the device was measured using a digital power meter at 60 mW. The laser coupling experiment (section 5.2) implies an approximate laser transmission inside the channel of 80% (assuming that the power losses over the channel are linearly related to the power inside the channel). This assumption results in an estimated laser power inside the channel of 48 mW (80% of 60 mW). To calculate the intensity distribution of the transmitted laser power we used this equation,

$$I = \frac{P}{\pi(r_{beam})^2}, \quad (5.2)$$

where the beam radius (r_{beam}) was measured as 20 μm , using the relative widths of the beam and channel. Using equation 5.2 the intensity distribution was calculated as **382 W/cm²**.

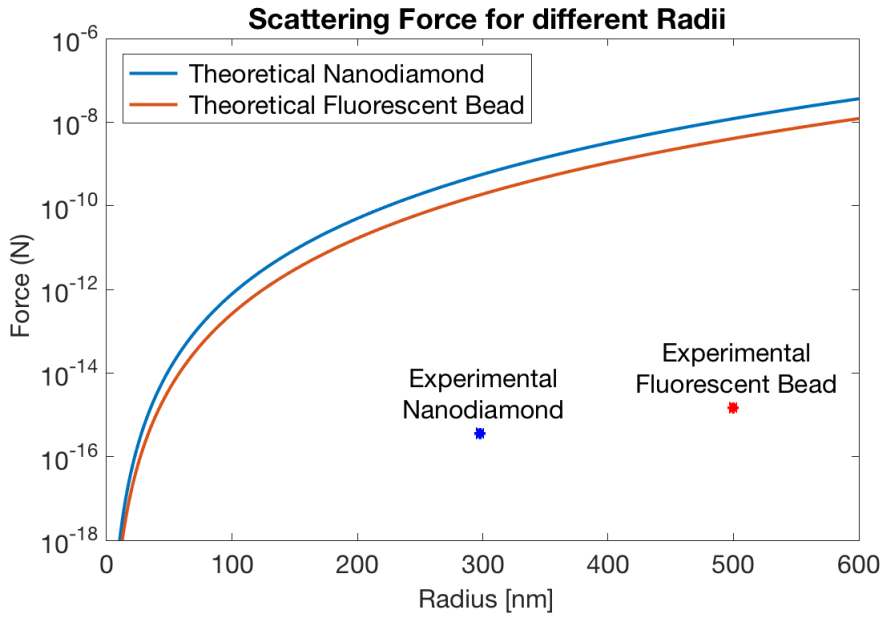


Figure 5.6: The experimental and theoretical scattering forces versus radius. The theoretical plot used the intensity distribution from 5.4.3 and the equation for bulk scattering cross section (equation 2.4) to calculate the theoretical force on the particle. This plot shows a large discrepancy between the magnitudes of the theoretical and experimental force, indicative of a problem with the model.

5.4.4 Calculation of the Scattering Cross Section

We used the experimental scattering force and the calculated intensity distribution to calculate the experimental scattering cross section using equation 5.3. These results are presented in table 5.2. The experimental values for the scattering force (F_{scat}) from 5.4.2 and Intensity distribution (I) from 5.4.3, were used to calculate the scattering cross section using a rearrangement of equation 2.3,

$$\sigma = \frac{2F_{scat}}{I}. \quad (5.3)$$

The theoretical value was calculated using equation 2.4.

Table 5.2: Scattering Cross Section for the Tested Particles

Particle Type	Nanodiamond	Fluorescent Bead
Refractive Index	2.42	1.59
Cross Sectional Area	17.4 fm ²	49.1 fm ²
Theoretical Scattering Cross Section	440 zm ²	3300 zm ²
Experimental Scattering Cross Section	0.019 zm ²	0.078 zm ²

5.5 Discussion

The calculation of the scattering force highlighted a difference between the expected results and the experimental results. This discrepancy could arise from problems with our model or experimental procedure. The first issue with the model is that it introduced an overestimation of the intensity distribution as it assumes the particle is at the focus of the beam waist. Using our setup it was difficult to account for particle movement (due to diffusion and flow) as the beam waist was significantly larger than the particle ($0.25\ \mu\text{m}$ particle radius (a) in a $20\ \mu\text{m}$ beam waist (r_{beam})). The experiment procedure was also flawed in that it was reliant on the users ability to track the particle along the channel length. The relative size of the particle and the inefficiencies of the laser movement decreased the intensity distribution that each particle experienced experimentally.

The theoretical model used the assumption that the experiment operated in the Rayleigh regime. The model for scattering force assumed that the small dielectric particles had a radius that was significantly smaller than the lasers wavelength ($a \ll \lambda$). This model will hold for the ND particles that the project aims to sort (particles with a $5\ \text{nm}$ radius) but it struggles to predict the effect of the force when the particle size is closer to the lasers wavelength (particles with a $500\ \text{nm}$ radius). We believe that the radii of the tested particles were responsible for a large proportion of the discrepancy due to the a^6 term in the equation for bulk scattering cross section (equation 2.4).

To improve the setup for future contributors, we recommend that a microscope chassis be placed on the optical table to establish a confocal setup and improve the image quality. A confocal setup with a sharper image would enable the tracking of smaller particles that could be processed using an automatic particle tracker.

These results do not discourage our project, we believe that the preliminary results have enabled the observation of a scattering force in an optofluidic environment. The DRIE microfluidic device exhibited excellent optical coupling. The group will continue to test the scattering force in DRIE devices to characterise the forces associated with the near resonant green laser. The experiment highlighted that most of the particles are diffusing inside the channel, while a few experienced a scattering force. Future experiments will need to characterise whether the particles that experience limited scattering are inherent or indicative of an inefficiency in the setup.

5.6 Chapter Summary

This chapter quantified the systems performance in the two experiments. These experiments were used to understand the optical coupling into the channel and the strength of the scattering force on suspended nanoparticles. This chapter concluded that the size of the theoretical scattering force was overestimated in our models, due to the assumed strength of the intensity distribution and a breakdown of the theoretical model as the particle size approached the illuminating wavelength. We also concluded that the inefficiencies of the optical setup decreased the scattering force experienced by impacted particles.

6

Conclusion

Over this year we established an optofluidic setup that impacted particles with a scattering force, this represented a significant step towards the realisation of our sorting mechanism. In this document the microfluidic fabrication chapter, outlined the design of three types of device to find a fabrication that created a device with effective optical coupling. The optical configuration chapter, described the optical path that was used to impact nanodiamonds inside the channel with a scattering force. The results chapter tested the optical coupling and laser scattering of the different fabrications. The optical coupling experiment highlighted the ability of the laser to travel through different types of fabrication. The laser scattering experiment was able to quantify the effect a near infrared laser had on different nanoparticles, we did not have time to test the scattering effect that was associated with a green laser.

To gain a more robust understanding of the scattering force effect, we will continue to measure the scattering effect using a variety of laser settings. We are confident that the discrepancies between the expected behaviour and experimental performance of the system will be improved with a more robust model and complete setup. This project will continue to develop as a collaborative effort over the coming years.

References

- [1] J. M. White. *Quantification Of Scattering Forces In A Microfluidic Channel* (2016).
- [2] A. M. Schrand, H. Huang, C. Carlson, J. J. Schlager, E. ÅÑsawa, S. M. Hussain, and L. Dai. *Are diamond nanoparticles cytotoxic?* The Journal of Physical Chemistry B **111**(1), 2 (2007).
- [3] P. Reineck, A. Francis, A. Orth, D. W. M. Lau, R. D. V. Nixon Luke, I. D. Rastogi, W. A. W. Razali, N. M. Cordina, L. M. Parker, V. K. A. Sreenivasan, L. J. Brown, and B. C. Gibson. *Brightness and photostability of emerging red and near ir fluorescent nanomaterials for bioimaging.* Advanced Optical Materials **4**(10), 1549 1557 (2016).
- [4] R. S. Balmer, J. R. Brandon, S. L. Clewes, H. K. Dhillon, J. M. Dodson, I. Friel, P. N. Inglis, T. D. Madgwick, M. L. Markham, T. P. Mollart, N. Perkins, G. A. Scarsbrook, D. J. Twitchen, A. J. Whitehead, J. J. Wilman, and S. M. Woollard. *Chemical vapour deposition synthetic diamond: materials, technology and applications.* Journal of Physics: Condensed Matter **21**(36), 364221 (2009).
- [5] F. P. Bundy, H. T. Hall, H. M. Strong, and R. H. Wentorf. *Man-made diamonds.* Nature **176**(4471), 51 (1955).
- [6] O. A. Shenderova and G. E. McGuire. *Science and engineering of nanodiamond particle surfaces for biological applications (review).* Biointerphases **10**(3), 030802 (2015).
- [7] O. A. Shenderova and S. A. Ciftan Hens. *Detonation nanodiamond particles processing, modification and bioapplications.* Nanodiamonds pp. 79–116 (2010).
- [8] I. D. Rastogi. *Luminescent Nanodiamonds As Biolabels.* Ph.D. thesis, Macquarie University (2016).

- [9] M. W. Doherty, N. Manson, P. Delaney, and L. Hollenberg. *The negatively charged nitrogen-vacancy centre in diamond: the electronic solution*. New Journal of Physics **13**, 1 (2011).
- [10] U. F. S. D’Haenens-Johansson, A. M. Edmonds, B. L. Green, M. E. Newton, G. Davies, P. M. Martineau, R. U. A. Khan, and D. J. Twitchen. *Optical properties of the neutral silicon split-vacancy center in diamond*. Phys. Rev. B **84**, 245208 (2011).
- [11] K. Bakowicz and S. Mitura. *Biocompatibility of ncd*. Journal of Wide Bandgap Materials **9**(4), 261 (2002).
- [12] V. Vaijayanthimala, Y.-K. Tzeng, H.-C. Chang, and C.-L. Li. *The biocompatibility of fluorescent nanodiamonds and their mechanism of cellular uptake*. Nanotechnology **20**(42), 425103 (2009).
- [13] C. Bradac, J. M. Say, I. D. Rastogi, N. M. Cordina, T. Volz, and L. J. Brown. *Nano-assembly of nanodiamonds by conjugation to actin filaments*. Journal of Biophotonics **9**(3), 296 (2016).
- [14] J. M. Say, C. van Vreden, D. J. Reilly, L. J. Brown, J. R. Rabeau, and N. J. C. King. *Luminescent nanodiamonds for biomedical applications*. Biophysical Reviews **3**(4), 171 (2011).
- [15] K. B. Holt. *Diamond at the nanoscale: applications of diamond nanoparticles from cellular biomarkers to quantum computing*. Philosophical Transactions of the Royal Society A: Mathematical, Physical and Engineering Sciences **365**(1861), 2845 (2007).
- [16] P. Reineck, A. Francis, A. Orth, D. W. M. Lau, R. D. V. Nixon-Luke, I. D. Rastogi, W. A. W. Razali, N. M. Cordina, L. M. Parker, V. K. A. Sreenivasan, L. J. Brown, and B. C. Gibson. *Brightness and photostability of emerging red and near-ir fluorescent nanomaterials for bioimaging*. Advanced Optical Materials **4**(10), 1549 (2016).
- [17] W. W. W. Hsiao, Y. Y. Hui, P. C. Tsai, and H. C. Chang. *Fluorescent nanodiamond: A versatile tool for long term cell tracking, super resolution imaging, and nanoscale temperature sensing*. Accounts of Chemical Research **49**(3), 400 407 (2016). PMID: 26882283.

- [18] I. I. Vlasov, A. A. Shiryaev, T. Rendler, S. Steinert, S. Y. Lee, D. Antonov, M. Voros, F. Jelezko, A. V. Fisenko, L. F. Semjonova, J. Biskupek, U. Kaiser, O. I. Lebedev, I. Sildos, P. R. Hemmer, V. I. Konov, A. Gali, and J. Wrachtrup. *Molecular sized fluorescent nanodiamonds*. *Nat Nano* **9**(1), 54–58 (2014).
- [19] C. Wyatt Shields IV, C. D. Reyes, and G. P. López. *Microfluidic cell sorting: a review of the advances in the separation of cells from debulking to rare cell isolation*. *Lab Chip* **15**(5), 1230 (2015).
- [20] B. Landenberger, H. Höfemann, S. Wadle, and A. Rohrbach. *Microfluidic sorting of arbitrary cells with dynamic optical tweezers*. *Lab on a Chip* **12**(17), 3177 (2012).
- [21] R. W. Applegate Jr., J. Squier, T. Vestad, J. Oakey, D. W. M. Marr, P. Bado, M. A. Dugan, and A. A. Said. *Microfluidic sorting system based on optical waveguide integration and diode laser bar trapping*. *Lab on a Chip* **6**(3), 422 (2006).
- [22] M. Xavier, R. O. Oreffo, and H. Morgan. *Skeletal stem cell isolation: A review on the state-of-the-art microfluidic label-free sorting techniques*. *Biotechnology Advances* **34**(5), 908 (2016).
- [23] J. D. Adams, U. Kim, and H. T. Soh. *Multitarget magnetic activated cell sorter*. *Proceedings of the National Academy of Sciences* **105**(47), 18165 (2008).
- [24] M. E. Warkiani, G. Guan, K. B. Luan, W. C. Lee, A. A. S. Bhagat, P. Kant Chaudhuri, D. S.-W. Tan, W. T. Lim, S. C. Lee, and P. C. Y. e. a. Chen. *Slanted spiral microfluidics for the ultra-fast, label-free isolation of circulating tumor cells*. *Lab Chip* **14**(1), 128 (2014).
- [25] T. Jing, R. Ramji, M. E. Warkiani, J. Han, C. T. Lim, and C.-H. Chen. *Jetting microfluidics with size-sorting capability for single-cell protease detection*. *Biosensors and Bioelectronics* **66**, 19 (2015).
- [26] X. Li, W. Chen, G. Liu, W. Lu, and J. Fu. *Continuous-flow microfluidic blood cell sorting for unprocessed whole blood using surface-micromachined microfiltration membranes*. *Lab Chip* **14**(14), 2565 (2014).
- [27] H. Song, J. M. Rosano, Y. Wang, C. J. Garson, B. Prabhakar Pandian, K. Pant, G. J. Klarmann, A. Perantoni, L. M. Alvarez, and E. Lai. *Continuous-flow sorting of stem*

- cells and differentiation products based on dielectrophoresis*. Lab Chip **15**(5), 1320 (2015).
- [28] A. H. J. Yang and H. T. Soh. *Acoustophoretic sorting of viable mammalian cells in a microfluidic device*. Analytical Chemistry **84**(24), 10756 (2012).
- [29] F. Paul, S. Roath, D. Melville, D. Warhurst, and J. Osisanya. *Separation of malaria-infected erythrocytes from whole blood: Use of a selective high-gradient magnetic separation technique*. The Lancet **318**(8237), 70 (1981).
- [30] L. Dong, D.-W. Chen, S.-J. Liu, and W. Du. *Automated chemotactic sorting and single-cell cultivation of microbes using droplet microfluidics*. Scientific Reports **6**(1) (2016).
- [31] Y. Harada and T. Asakura. *Radiation forces on a dielectric sphere in the rayleigh scattering regime*. Optics Communications **124**, 529 (1996).
- [32] Y. Zhang and B. Li. *Particle sorting using a subwavelength optical fiber*. Laser and Photonics Reviews **7**(2), 289 (2013).
- [33] M. Ploschner, T. Cizmár, M. Mazilu, A. Di Falco, and K. Dholakia. *Bidirectional optical sorting of gold nanoparticles*. Nano Letters **12**(4), 1923 (2012).
- [34] K. D. Leake, B. S. Phillips, T. D. Yuzvinsky, A. R. Hawkins, and H. Schmidt. *Optical particle sorting on an optofluidic chip*. Optics Express **21**(26), 32605 (2013).
- [35] G. Grynberg, A. Aspect, C. Fabre, and Cohen-Tannoudji. *Introduction to Quantum Optics* (Cambridge University Press, 2010, 2010).
- [36] K. C. Neuman and S. M. Block. *Optical trapping*. Review of scientific instruments **75**(9), 2787 (2004).
- [37] R. H. Dicke. *Coherence in spontaneous radiation processes*. Phys. Rev. **93**, 99 (1954).
- [38] C. D. Aiello. *Optical dipole forces: Working together* (2017).
- [39] M. Juan, C. Bradac, B. Besga, M. Johnsson, G. Brennen, G. Molina-Terriza, and T. Volz. *Cooperatively enhanced dipole forces from artificial atoms in trapped nanodiamonds*. Nature Physics **13**(3), 241 (2016).

- [40] G. M. Whitesides. *The origins and the future of microfluidics*. Nature **442**(7101), 368 (2006).
- [41] K. F. Lei. *Chapter 1 Materials and Fabrication Techniques for Nano- and Microfluidic Devices* (The Royal Society of Chemistry, 2015).
- [42] C. D. Chin, V. Linder, and S. K. Sia. *Commercialization of microfluidic point-of-care diagnostic devices*. Lab on a Chip **12**(12), 2118 (2012).
- [43] E. K. Sackmann, A. L. Fulton, and D. J. Beebe. *The present and future role of microfluidics in biomedical research*. Nature **507**(7491), 181 (2014).
- [44] J. Chen, J. Li, and Y. Sun. *Microfluidic approaches for cancer cell detection, characterization, and separation*. Lab on a Chip **12**(10), 1753 (2012).
- [45] H. N. Joensson and H. AnderssonSvahn. *Droplet microfluidics-a tool for single-cell analysis*. Angewandte Chemie International Edition **51**(49), 12176 (2012).
- [46] P. Neuÿi, S. Giselsbrecht, K. Lange, T. J. Huang, and A. Manz. *Revisiting lab-on-a-chip technology for drug discovery*. Nature Reviews Drug Discovery **11**(8), 620 (2012).
- [47] K. Ren, J. Zhou, and H. Wu. *Materials for microfluidic chip fabrication*. Accounts of Chemical Research **46**(11), 2396 (2013).
- [48] B. L. Thompson, Y. Ouyang, G. R. M. Duarte, E. Carrilho, S. T. Krauss, and J. P. Landers. *Inexpensive, rapid prototyping of microfluidic devices using overhead transparencies and a laser print, cut and laminate fabrication method*. Nature Protocols **10**(6), 875 (2015).
- [49] Y. Yalikun, N. Tanaka, Y. Hosokawa, T. Iino, and Y. Tanaka. *Ultrathin glass filter fabricated by femtosecond laser processing for high-throughput microparticle filtering*. Applied Physics Express **9**(6), 066702 (2016).
- [50] R. Chutani, M. Hasegawa, V. Maurice, N. Passilly, and C. Gorecki. *Single-step deep reactive ion etching of ultra-deep silicon cavities with smooth sidewalls*. Sensors and Actuators A: Physical **208**, 66 (2014).
- [51] T. M. Adams and R. A. Layton. *Introductory MEMS: Fabrication and Applications* (Springer US: Boston, MA, Boston, MA, 2010).

-
- [52] L. Akesso. *Gm1070 technical datasheet*. URL <http://www.gersteltec.ch/userfiles/1197841378.pdf>.
- [53] P. Targowski, R. Ostrowski, J. Marczak, M. Sylwestrzak, and E. A. Kwiatkowska. *Picosecond laser ablation system with process control by optical coherence tomography*. Proc.SPIE **7391**, 7391 (2009).
- [54] O. Ertl and S. Selberherr. *Three-dimensional level set based bosch process simulations using ray tracing for flux calculation*. Microelectronic Engineering pp. 20–29 (2013).
- [55] E. Committee. *Microelectronics Failure Analysis: Desk Reference*. Microelectronics Failure Analysis: Desk Reference (ASM International, 2004).
- [56] D. W. Inglis. *A method for reducing pressure-induced deformation in silicone microfluidics*. Biomicrofluidics **4**(2), 026504 (2010).
- [57] T. Glawdel, Z. Almutairi, S. Wang, and C. Ren. *Photobleaching absorbed rhodamine b to improve temperature measurements in pdms microchannels*. Lab Chip **9**, 171 (2009).
- [58] M. D. Abramoff. *Image processing with imagej*. Biophotonics International **11**(7), 36 (2004).